GEOLOGICAL SURVEY OF CANADA
OPEN FILE 8529

2017 Korea-Canada-U.S.A. Beaufort Sea (offshore Yukon and Northwest Territories) research program: processing of 2-D seismic data collected during expedition ARA08C

M.J. Duchesne, S.-G. Kang, and U. Jang

2019

Canada

GEOLOGICAL SURVEY OF CANADA
OPEN FILE 8529

2017 Korea-Canada-U.S.A. Beaufort Sea (offshore Yukon and Northwest Territories) research program: processing of 2-D seismic data collected during expedition ARA08C

M.J. Duchesne[1], S.-G. Kang[2], and U. Jang[2]

[1] Geological Survey of Canada, 490, rue de la Couronne, Québec, Quebec G1K 9A9
[2] Korea Polar Research Institute, Division of Polar Earth-System Sciences, 26 Songdomirae-ro, Yeonsu-gu, Incheon (21990), Korea

2019

Permanent link: https://doi.org/10.4095/313533

This publication is available for free download through GEOSCAN (http://geoscan.nrcan.gc.ca/).

Publications in this series have not been edited; they are released as submitted by the author.

ABSTRACT

During expedition ARA08C, 890 km of multichannel seismic data have been collected offshore Yukon and Northwest Territories in water depths ranging from 23 to 1866 m onboard RV Araon operated by the Korea Polar Research Institute. The layout of the seismic program was designed to address a wide variety of geological problems including subsea permafrost, gas hydrates, glacial history, fluid migration and offshore geohazards. The survey provided a very high quality dataset but shallow water depths and hard sea bottom made the processing of the seismic data challenging. This report highlights processing methods applied on the dataset and briefly discusses processing results in terms of improvement of the subsurface imaging.

RÉSUMÉ

Au cours de l'expédition ARA08C, 890 km de données sismiques multicanaux ont été acquis au large des côtes du Yukon et des Territoires du Nord-Ouest par des profondeurs d'eau allant de 23 à 1866 m à bord du NR Araon opéré par l'Institut de Recherche Polaire de Corée. Le programme de levé sismique a été conçu pour aborder une grande variété de problèmes géologiques, notamment le pergélisol sous-marin, les hydrates de gaz, l'histoire des glaciations, la migration des fluides et les géorisques extracôtiers. La campagne a fourni un ensemble de données de très haute qualité, mais la faible profondeur d'eau et le fond marin dur ont compliqué le traitement des données sismiques. Ce rapport met en évidence les méthodes de traitement appliquées à l'ensemble de données et discute brièvement des résultats de ce traitement en termes d'amélioration de l'imagerie en sous-surface.

INTRODUCTION

The Korea Polar Research Institute (KOPRI) is engaged in a long-term collaborative research agreement with the Geological Survey of Canada (GSC), the Monterey Bay Aquarium Research Institute (MBARI) and the Department of Fisheries and Oceans (DFO). ARA08C is the third expedition onboard the icebreaker RV Araon operated by KOPRI in the Canadian Beaufort Sea and builds upon successes and lessons learn from expeditions ARA04C (2013) and ARA05C (2014) (Jin et al., 2015 and Jin et al., 2016). Scientific data collected are targeting topics such as degrading permafrost and gas hydrates in the outer shelf and upper slope, offshore geohazards, glacial history, paleoceanography, microbiology, the monitoring of the upper-ocean waters, atmospheric science and global climate change (Jin et al., 2018). More specifically, the contribution of multichannel seismic data (MCS) collected onboard the RV Araon target the characterization of changing subsea permafrost conditions, the identification of gas hydrate and shallow gas accumulations, fluid migration pathways, the imaging of late glacial features and seismic oceanography (see Géli et al., 2005).

GEOLOGICAL SETTING

The Canadian Beaufort Sea results from the formation of the Canada Basin initiated by a rifting episode at the early Cretaceous, followed by upper Cretaceous flooding and shales deposition derived largely from the south and into the Mackenzie Basin (Grantz et al., 2011). Then, further tectonism followed with input of unconformity and sequence-bounded mixed clastics from the Mackenzie River and the Amundsen Gulf between the early and mid-Cenozoic. Northerly-directed convergence succeeded this episode resulting in the formation of the Beaufort Foldbelt in the Mackenzie Valley region. An Oligocene pull-apart formed a deep basin beneath the Beaufort Shelf and local broad folding (Helwig et al., 2011). The upper stratigraphy of the Canadian Beaufort Sea

is dominated by a late Miocene unconformity overlain by a thick, prograding sequence of Plio-Pleistocene muds including deltaic bodies, shelf-edge facies and abundant mass failure. The stratigraphic units defined by Dixon et al. (1994) and Graves et al. (2010) include the Kugmallit Formation associated with the most recent pull-apart, the thick Mackenzie Bay (over the Miocene unconformity), followed by the equally thick Akpak Formation, and a Pliocene shelf-top wedge with thick and multiple-failed slope equivalents termed the Iperk Formation.

The shelf of the Canadian Beaufort Sea has a width of ~100 km and ~150km respectively off the coastline of the Yukon and Northwest Territories (Figure 1). At the mouth of the Mackenzie River the shelf is wider reaching ~165km. In the Mackenzie Trough, the stratigraphic units mentioned above have been incised, up to 300 m, by glaciations which largely filled this geological feature (Batchelor et al., 2013). The Canadian Beaufort Sea shelf has been inundated by seawater following the last glacial maximum (~26 KaBP (cal)) (Taylor et al., 2013). It is underlain by a thick and wide permafrost body that extends offshore until the shelf break is reached in ~100 m of water depth. Gas hydrates are also present beneath the Canadian Beaufort Sea shelf as low formation temperature allows them to remain stable at shallower depths they are usually observed. They are also documented in more classical settings at the shelf break and on the continental slope (Riedel et al., 2017). Permafrost thawing and gas hydrate dissociation in response to sea-level rise are known to occur in the area leading to gas venting and pingo-like features forming at the seafloor (Paull et al., 2007). These are cited as geological factors that contribute to a decrease in strength of near-surface sediments, explaining the abundant signatures of seabed instability in the Canadian Beaufort Sea (Blasco et al., 2013).

MULTICHANNEL SEISMIC DATA ACQUISITION
Twelve MCS lines have been collected over a 5-day program representing 890 line-km of seismic data and 35 496 shot points from August 31st to September 4 2017 (Figure 1; Jin et al. (2018)). Besides the first day where agitated sea conditions persisted, calm winds and flat seas dominated the remaining days of the survey leading to the acquisition of very high quality data. The seismic source is positioned 31.25 m behind the ship's stern, towed 6 m beneath the sea surface, and fired every 25 m. Seismic energy is generated by an airgun array of two 210 in^3 Sercel Generator-Injectors for a total source volume of 420 in^3. Seismic arrivals are recorded using a 1.75 km-long streamer that consisted in 150 m-long lead-in cable, 50-m long head-stretch, 10 150 m-long solid state active sections including 12 receiver groups spaced by 12.5 m and a tail buoy deployed at end of 50 m-long cable. Six birds are mounted every 300 m on the streamer to insure it was towed at a constant depth of 6 m. The nearest and the farthest offsets were respectively located 85 m and 1572.5 m behind the source. This survey configuration resulted in a fold of 30 (Figure 2). Shot files are recorded in SEG-D format at sample rate of 1 ms over a trace length of 8000 ms. The navigation was provided by the GPS antenna of the ship and positions were recorded for every shot point in a separate ASCII files.
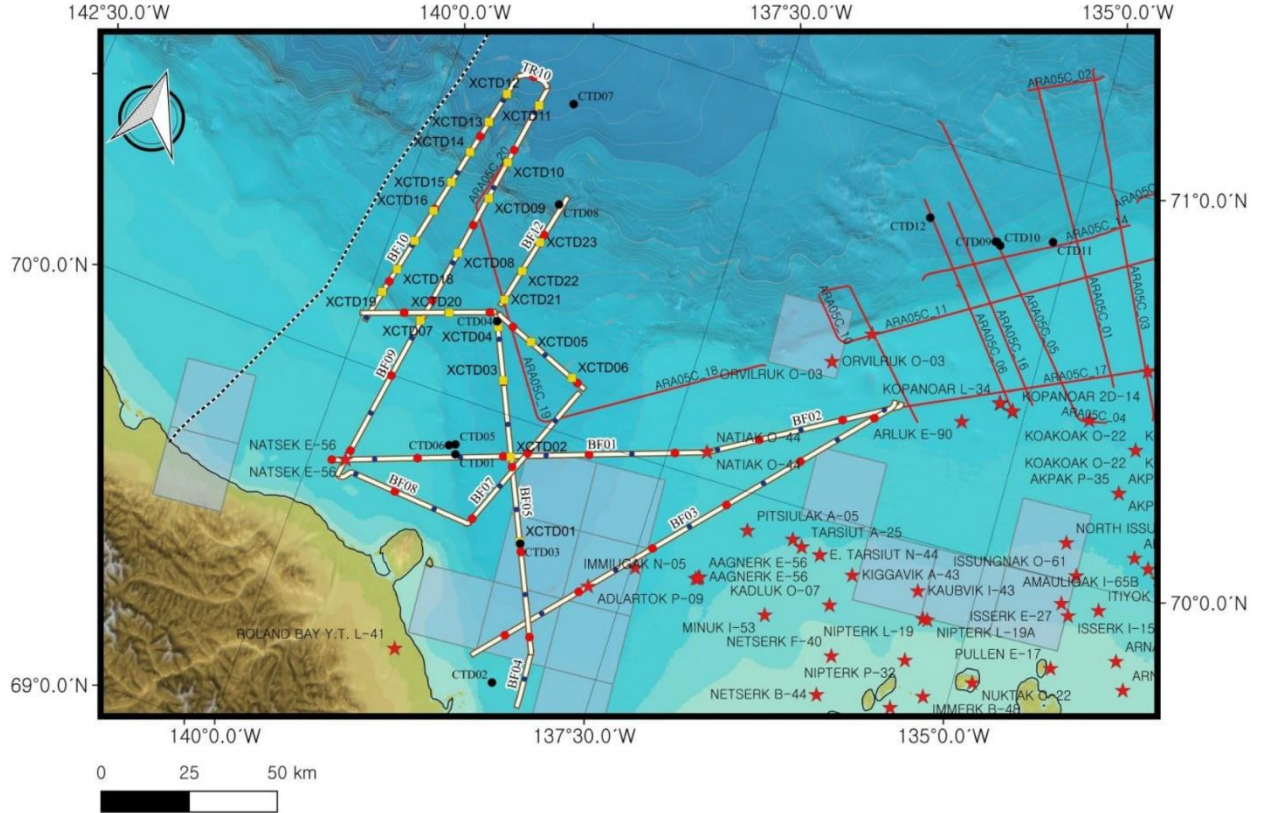
Figure 1. Seismic survey location map during cruise ARA08C (white solid lines: seismic lines; yellow circle: eXpendable Conductivity Temperature Depth (XCTD) probe stations; red circles: grid point in 1000th shot points; red stars: well sites) (From Jin et al., 2018).

MULTICHANNEL SEISMIC DATA PROCESSING

The processing flow includes 23 main steps (see Appendix 1). Each processing step is briefly described in terms of theory, and purpose. Prestack and stacked examples extracted from different lines are also used to discuss improvement in signal-to-noise ratio (s/n), coherency and subsurface imaging (Figure 1). Processing is performed on a DELL Precision tower 7910 equipped with two Intel-Xeon E5-2660v4 2.0 GHz processors totalizing 56 cores and a memory of 128 GB using Schlumberger's VISTA 2017 commercial software package running on a Windows 10 Enterprise operating system.
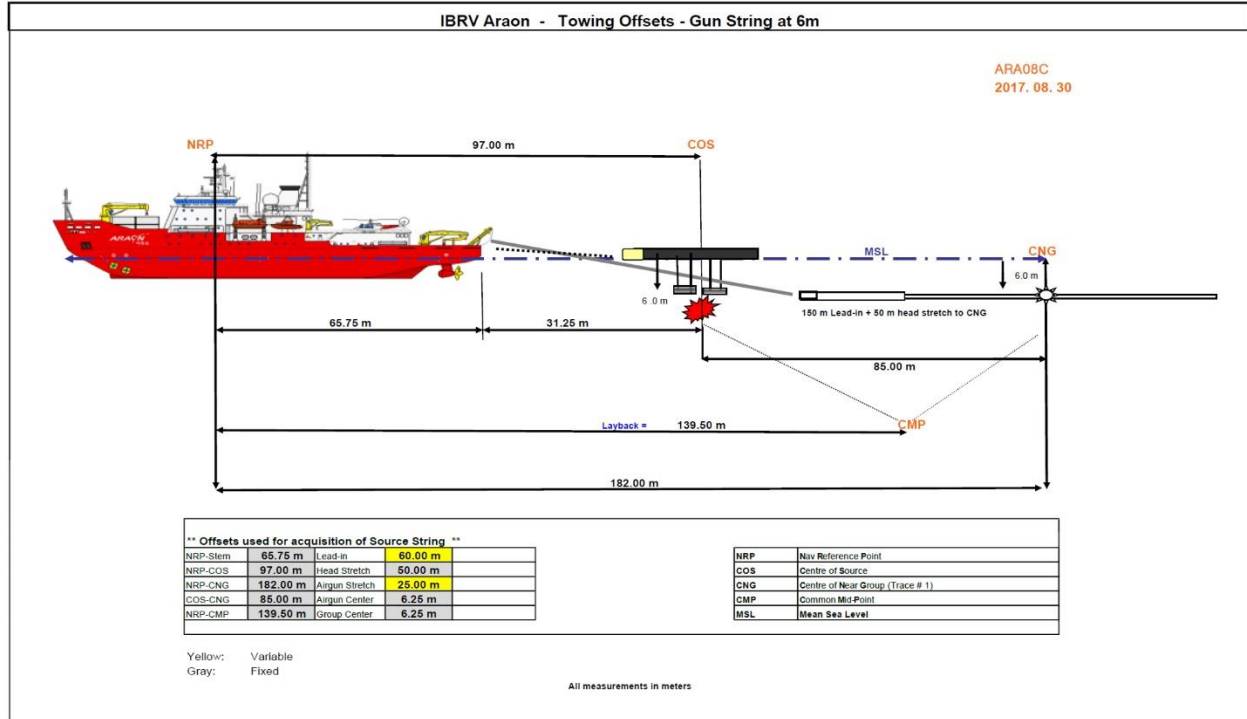
Figure 2. Field acquisition parameters and layouts (From Jin et al., 2018).

Input data

Raw data consisting of SEG-D shot gather files are initially converted to SEG-Y format and resampled from 1 ms to 2 ms. Resampling is used for data reduction. It did not alias the data as the seismic energy recorded is comprised between 5 and 120 Hz, thus significantly beyond the 500 Hz Nyquist frequency of the original sampling rate of 1 ms. Moreover, only the first 5000 ms of data are processed since no coherent reflected arrivals could be identified between 5000 and 8000 ms.

Figure 3 shows a typical shot gather recorded in ~65 m of water depth. The shot gather contains notable swell noise in the near to mid-offset range, characterized by high amplitude and low frequency energy. Figure 3b) presents a zoom-in of the shot gather over 0-2000 ms time-window using a 1000 ms AGC function for display purposes where several arrivals are identified. One can see that the direct arrival crosscuts shallow reflected events across almost all the offsets from 180 to 1175 ms. Refracted arrivals having a velocity of 1825 m s^{-1} also appear in the mid-offset range. Surface waves are also reverberating along the gather as low amplitude and low frequency events. The first free surface multiple that corresponds to a sharp high amplitude, reversed polarity event is imaged as well from the nearest offset to 472.5 m of offset before being interlaced with the direct arrival. Reflections appear as hyperbolic seismic events that are blurred by the low frequency component of the noise. The s/n of the raw shot gather is 0.51 meaning that noise is significantly more prominent than signal in the input data.
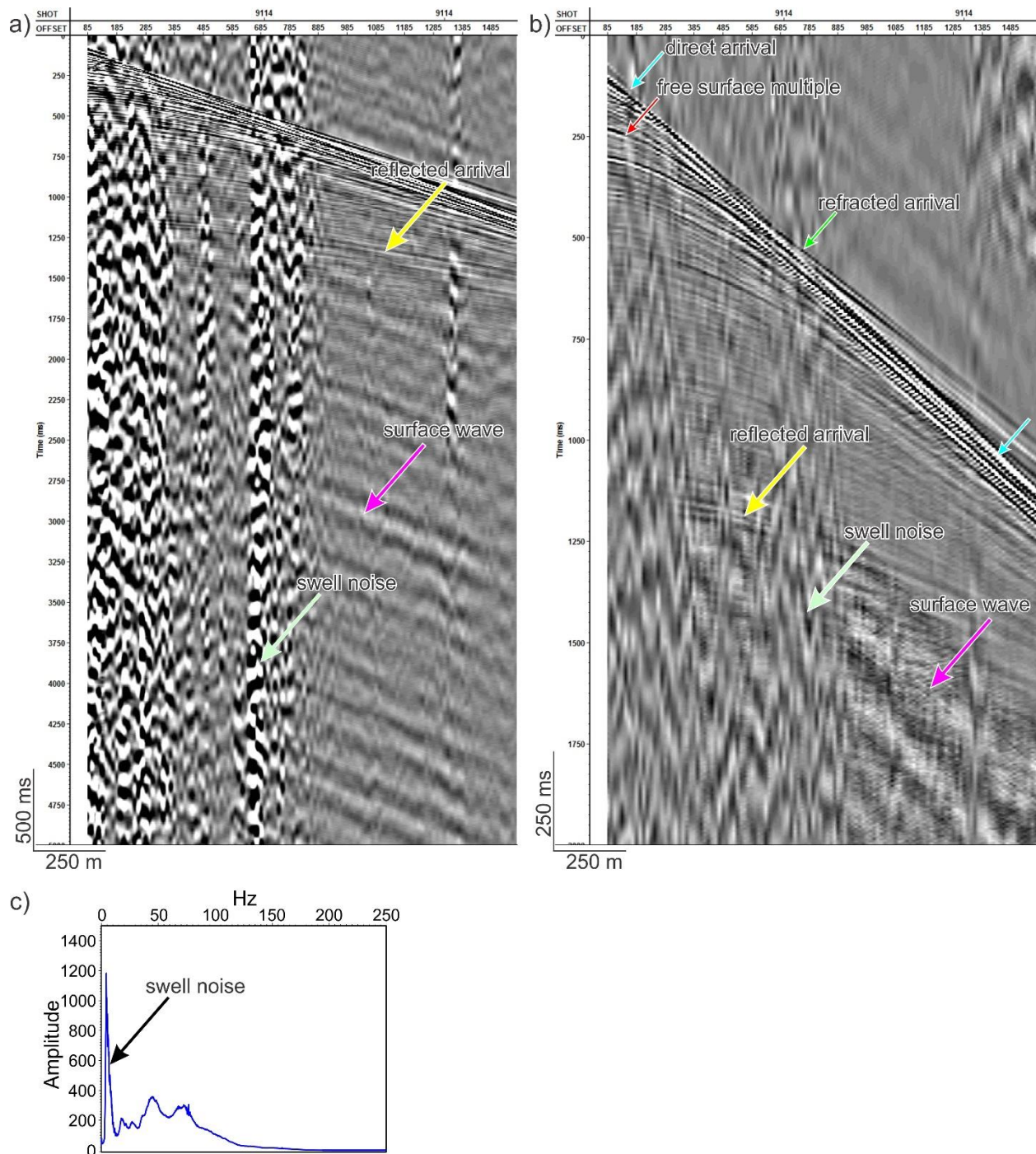
Figure 3. A typical shot gather recorded in shallow water depths a) full 5000 ms window display, b) zoom-in of the top 2000 ms and c) amplitude spectrum of a). On b) a 1000 ms AGC window is applied for display purposes so the high amplitude swell noise does not mask the different arrivals recorded.

Geometry editing

This step consists in associating each recorded trace with shot and receiver locations. Here shot and receivers positions are computed from an arbitrary origin of x=0 m and y=0 m since the streamer is not equipped of acoustic positioning transceivers for measuring ranges between each

5

channels and the survey vessel. Thus, a straight receiver configuration is assumed to bin the survey according to a bin size of 6.25m x 6.25m.

Spherical divergence correction
Raw data are corrected for spherical divergence to compensate the decrease of the energy of the seismic wavefront as it propagates downward into the Earth (Newman, 1973). This propagation involves a geometrical spreading that is associated with a decrease in energy density resulting in an amplitude loss that is inversely proportional to the distance from the source point to the wavefront. Data are corrected as a function of time and velocity. Figure 4 shows a shot gather before and after spherical divergence correction. As expected the amplitude of the early arrivals are lower and amplitude of the late arrivals are higher after applying the correction. This also valid for coherent and random noise. Most importantly, deeper reflections are now seen.

Swell noise attenuation
Swell noise is attenuated and replaced using a frequency domain median threshold filter that operates from short FFT windows so samples belonging to a single event are combined to insure that if the amplitudes are modified the output is still smooth in time (Butler, 2012). If the signal amplitude from a trace differs from the median by more than a predetermined threshold, the amplitude is progressively replaced with the median. Figure 5 presents the data before and after swell noise attenuation. The method efficiently attenuates the swell noise. Moreover, surface waves are attenuated as well. The amplitude spectra show that the noise is removed without altering the useful bandwidth of the data. The horizontal events crossing the gather correspond to a DC component recorded in the data that can be easily removed using a low-cut or a band-pass filter.

Direct arrival attenuation
Direct arrival attenuation is performed using a Frequency-wavenumber (FK) filter (Treitel, 1967). Before designing the FK filter, 2-D trace interpolation is conducted because the data suffered from wrap around aliasing that impeded the design of an optimal filter targeting the direct arrival (Figure 6). Thus, trace interpolation is achieved using an iterative process in the FK domain for creating a regularly sampled dataset using the approach of Khatchatrian (2012). Traces are interpolated over a bandwidth of 0 to 150 Hz and between wavenumbers 0.25 and 0.45 to generate an offset spacing of 6.25 m, increasing the numbers of channel to 240. After the trace interpolation, the direct arrival can be picked more easily for designing the FK filter (Figure 6). The FK representation of the shot
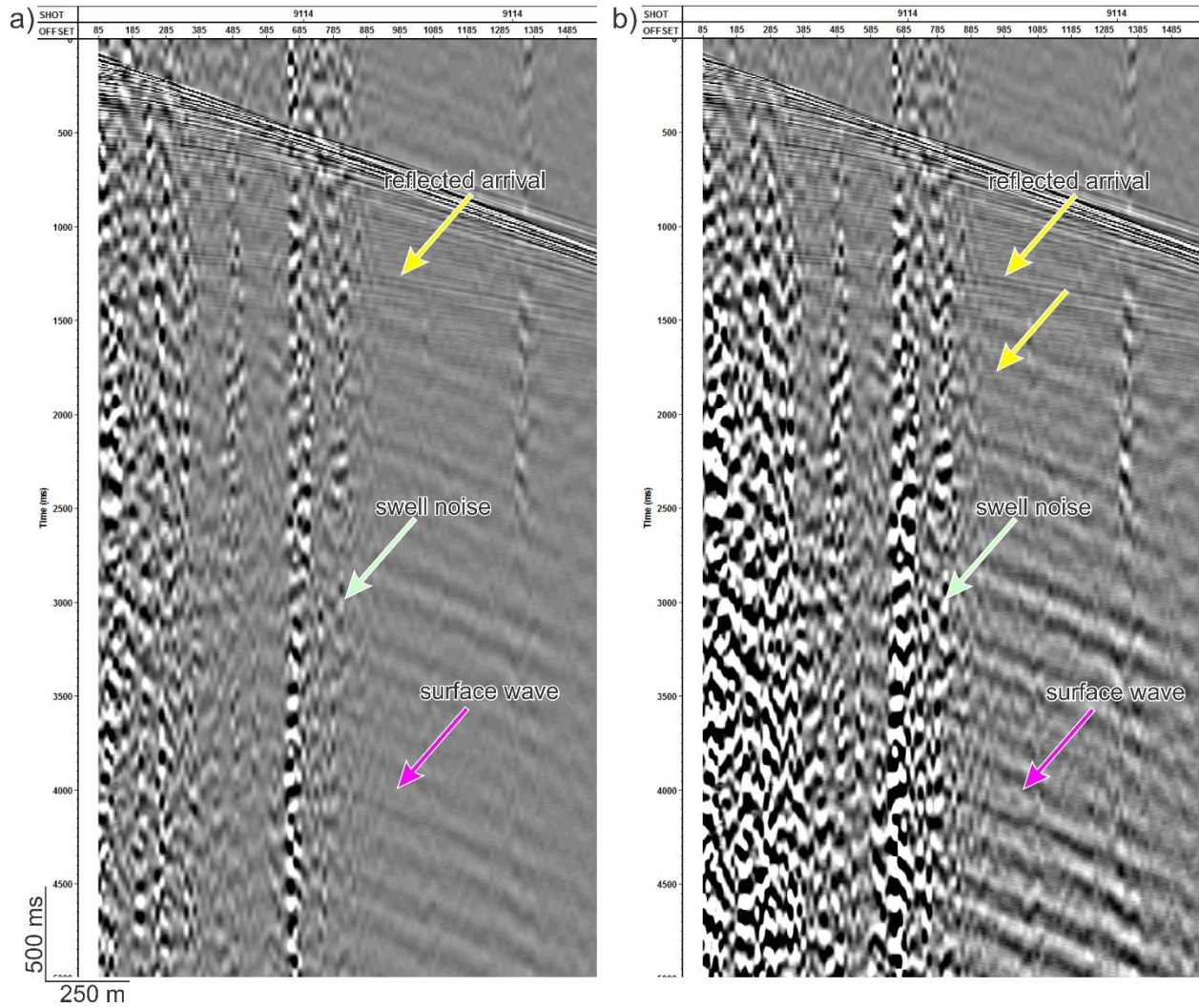
Figure 4. a) A shot gather before and b) after spherical divergence correction.

gather and interpolated shot gather also shows the energy of the DC component correlating with low frequencies and small wavenumbers. The hatched polygons on the FK representation of the interpolated shot gather correspond to the portions of FK window that are filtered out. The two dipping FK polygons between wavenumbers 0 and -0.5 and 0 and 0.5 are designed based on a velocity of 1430 m s^{-1} that is 20 m s^{-1} slower than the stacking velocity of a soft sea bottom in the Canadian Beaufort Sea. Figure 7 illustrates the result of the attenuation of the direct arrival and the DC component after the interpolated traces are removed. On Figure 7b, the cyan arrow points at far offsets where the energy of the direct arrival are significantly attenuated. The direct arrival energy is also attenuated in the mid-offset range (cyan arrow on Figure 7b) as some moveout can now be observed more easily. After application of the FK filter, diffracted energy recorded on the far offsets can be picked up with more ease than on Figure 7a. Figure 7c corresponds to the difference plot between shot gathers before and after FK filtering. The events on the plot are noise that have a slope equivalent to the direct arrival and the flat arrivals attributed to the DC component. Because the velocity of the direct arrival neighbours the velocity of the seafloor arrival and both events have energy spread over similar wavenumbers, harsher FK filtering could not be used.
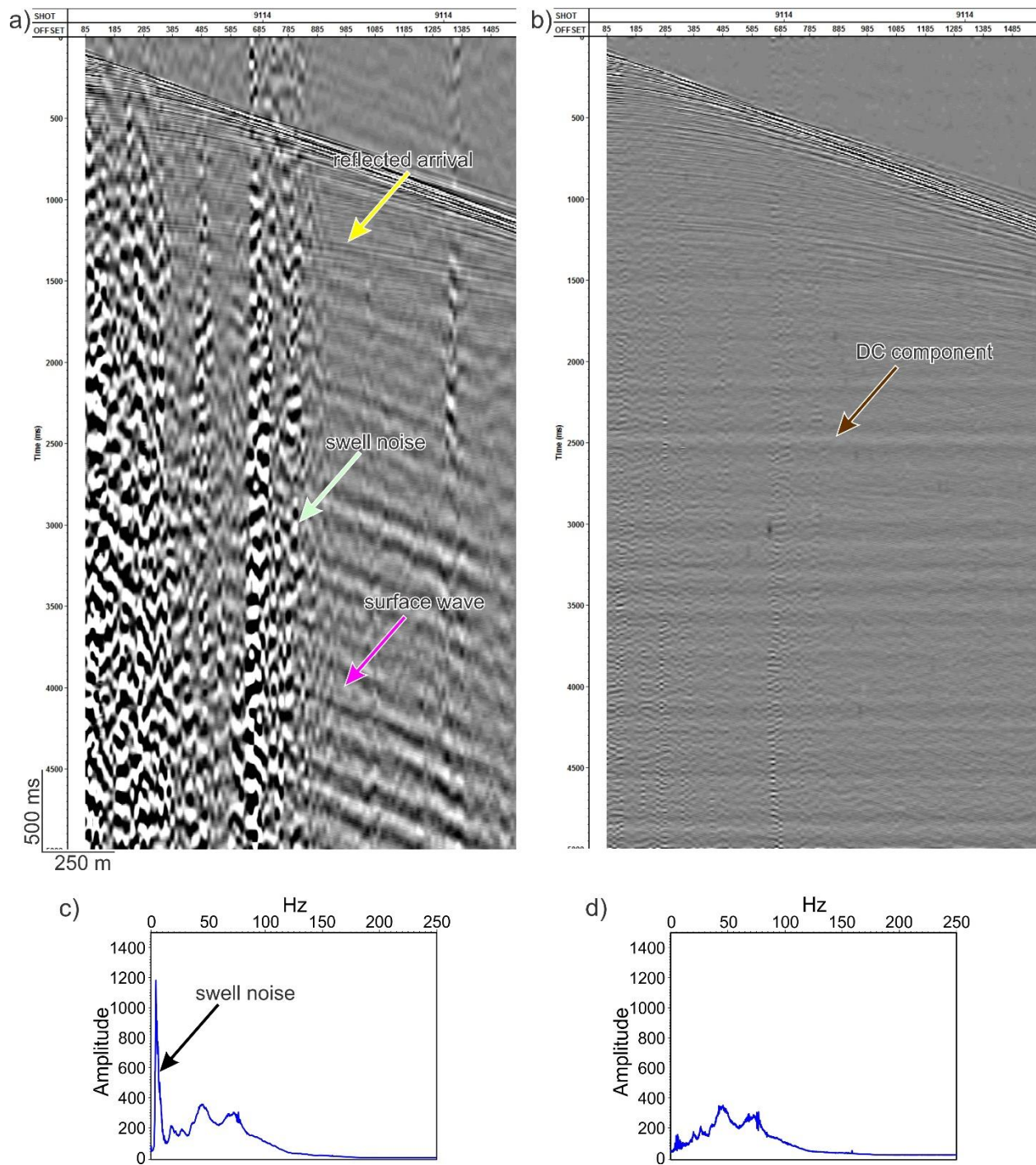
7

Figure 5. a) A shot gather before and b) after swell noise attenuation. c) and d) show amplitude spectra before and after swell noise attenuation respectively.
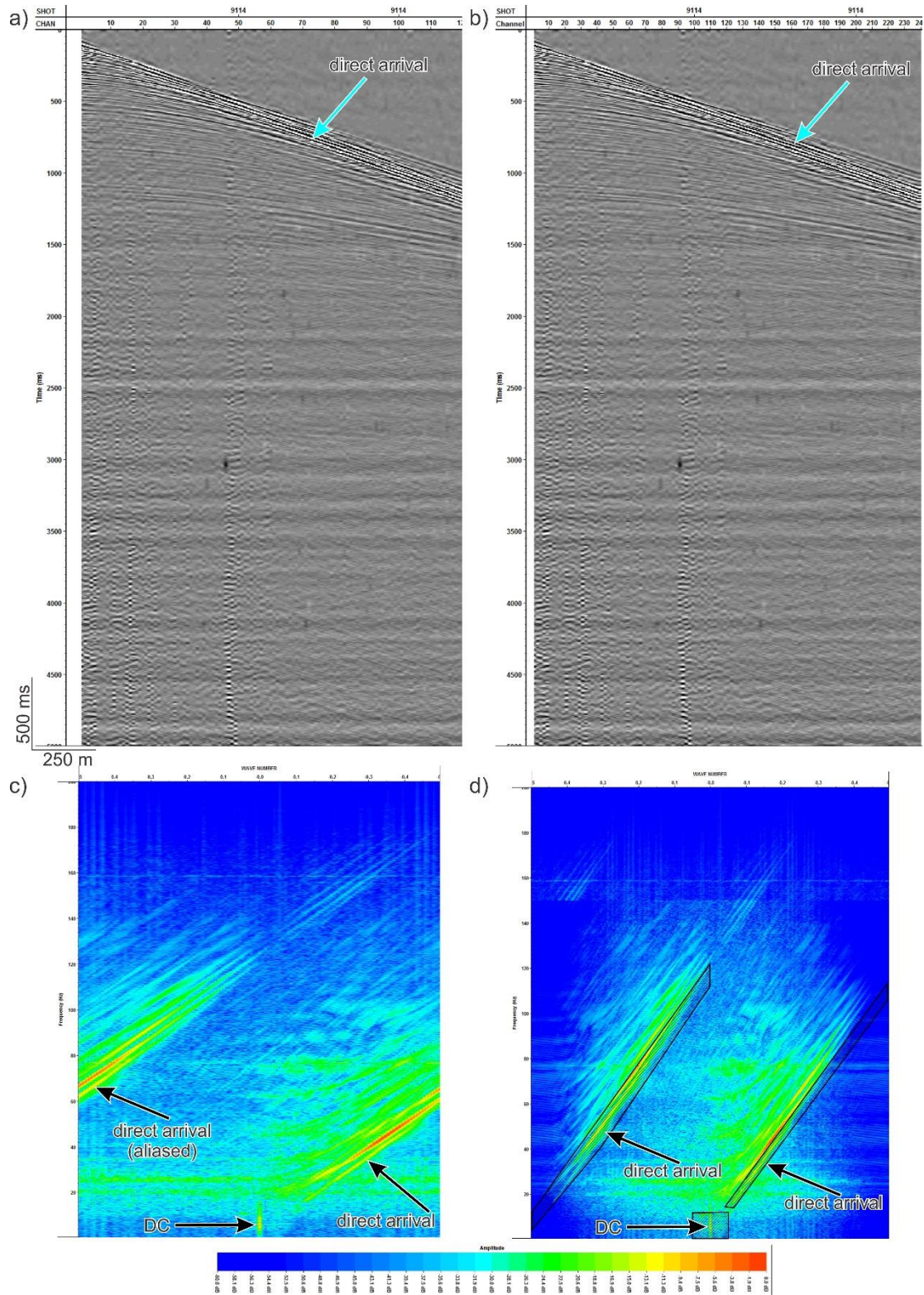
Figure 6. a) A shot gather before and b) after 2-D trace interpolation. c) and d) show FK spectra before and after 2-D trace interpolation respectively. Hatched polygons on d) correspond to portions of the FK spectrum that are muted to attenuate the direct arrival and the DC component
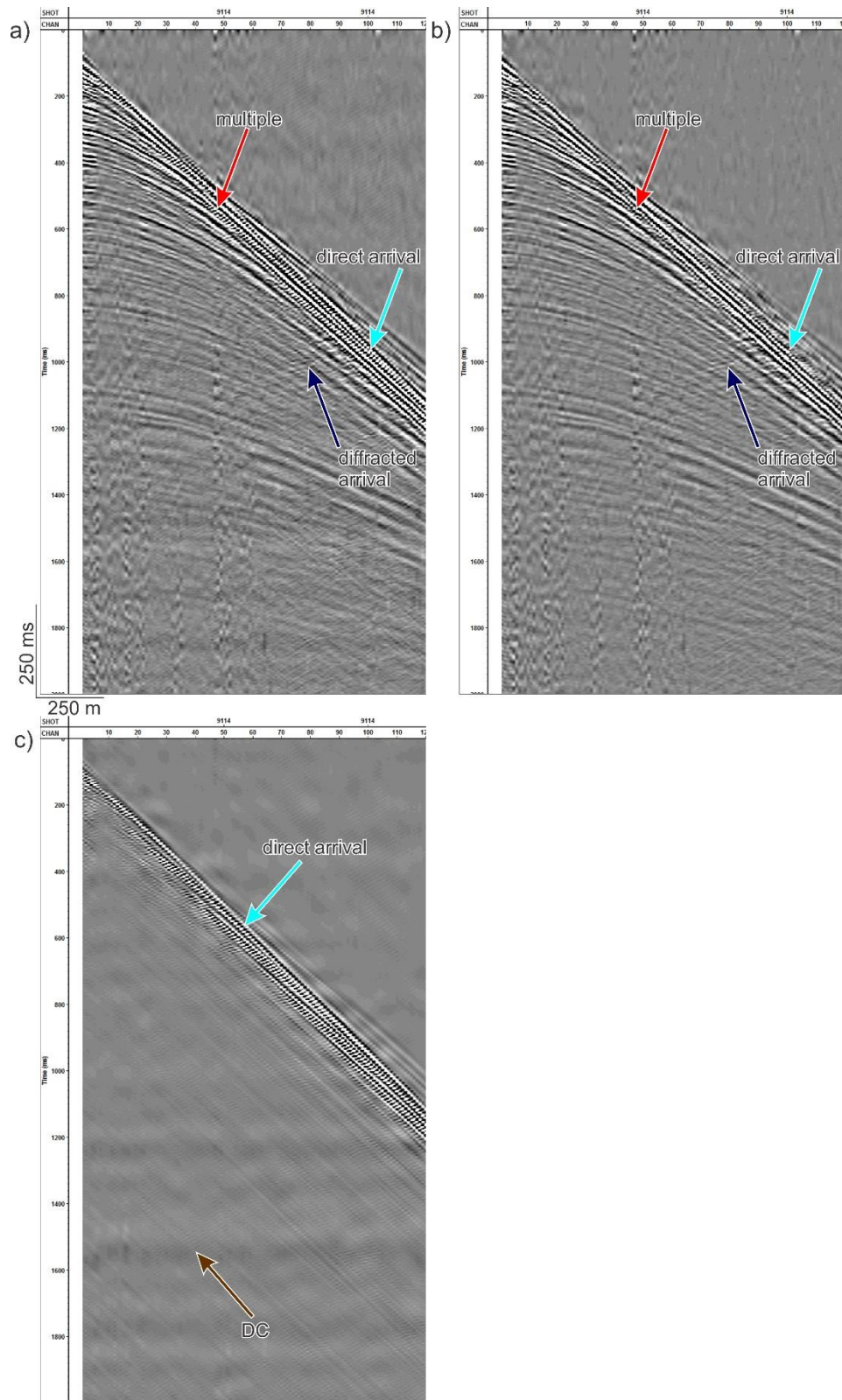
Figure 7. a) A shot gather before, b) after direct arrival attenuation and c) difference plot of a)-b).

Signature deconvolution

The source signature is very clean with a primary-bubble ratio of 7.6 because of the use of generator-injector airgun technology (see Pascouet, 1991) that greatly reduces the amplitude of bubble oscillations. Nevertheless, residual oscillations are recorded in the source wavelet. These are attenuated using the signature deconvolution approach of Wood et al. (1978). This deterministic deconvolution involves the computation of a zero-delay Wiener filter corresponding to the inverse of the source signature and that is matched-filter to obtain the autocorrelation of the source signature (or the signature deconvolution operator) that is cross-correlated with the seismic traces. Here the deconvolution operator is derived from the direct arrival recorded on the nearest offset (Figure 8a). Figure 8 shows a wiggle variable-area display of 80 traces recorded on the nearest offset (channel #1, 85 m) before (8b) and after (8c) signature deconvolution. The approach has significantly compressed the source signature, sharpening up reflected events. As a result, the amplitude spectrum is broadened towards the higher frequencies, improving the vertical resolution of the data (Figure 8d and e).

1st velocity analysis
This first velocity analysis is done in preparation of multiple attenuation. Before conducting velocity analysis, traces are sorted as CMP gathers. CMP gathers are filtered using Ormsby bandpass filter (10-30-80-100 Hz) and amplitudes are rescaled using a short time-window (250 ms) AGC scaling to respectively attenuate high-frequency random noise and increase the amplitude of the late arrivals. A top mute is also applied to zero out refracted arrivals. Velocity analysis are conducted every 100 CMPs using super-gathers that included 7 bins to increase the s/n. Velocities are picked on semblance gathers calculated for RMS velocities ranging from 1300 to 4500 m s^{-1} using a 5 m s^{-1} increment. Velocities could not be picked automatically using the maximal semblance values, because those are frequently correlative with free surface and internal multiples. Figure 9 presents a semblance gather used to pick the RMS velocities at a CMP location characterized by a hard sea bottom. Red arrows point at slow velocities attributed to free surface multiples that reverberate across the gather. Their RMS velocity of 1750 m s^{-1} is somewhat larger than what is expected, i.e. a seafloor velocity of 1450-1500 m s^{-1}. The velocity of 1750 m s^{-1} matches the velocity of a high amplitude event located <30 ms beneath the seafloor that also has an interval velocity of nearly 2000 m s^{-1}. Crimson arrows on the gather indicate high semblance values that are correlative to internal multiples that originate from large acoustic impedance contrasts. On the semblance gathers, RMS velocity inversion preceded by an increased in velocity are diagnostic of such multiples.
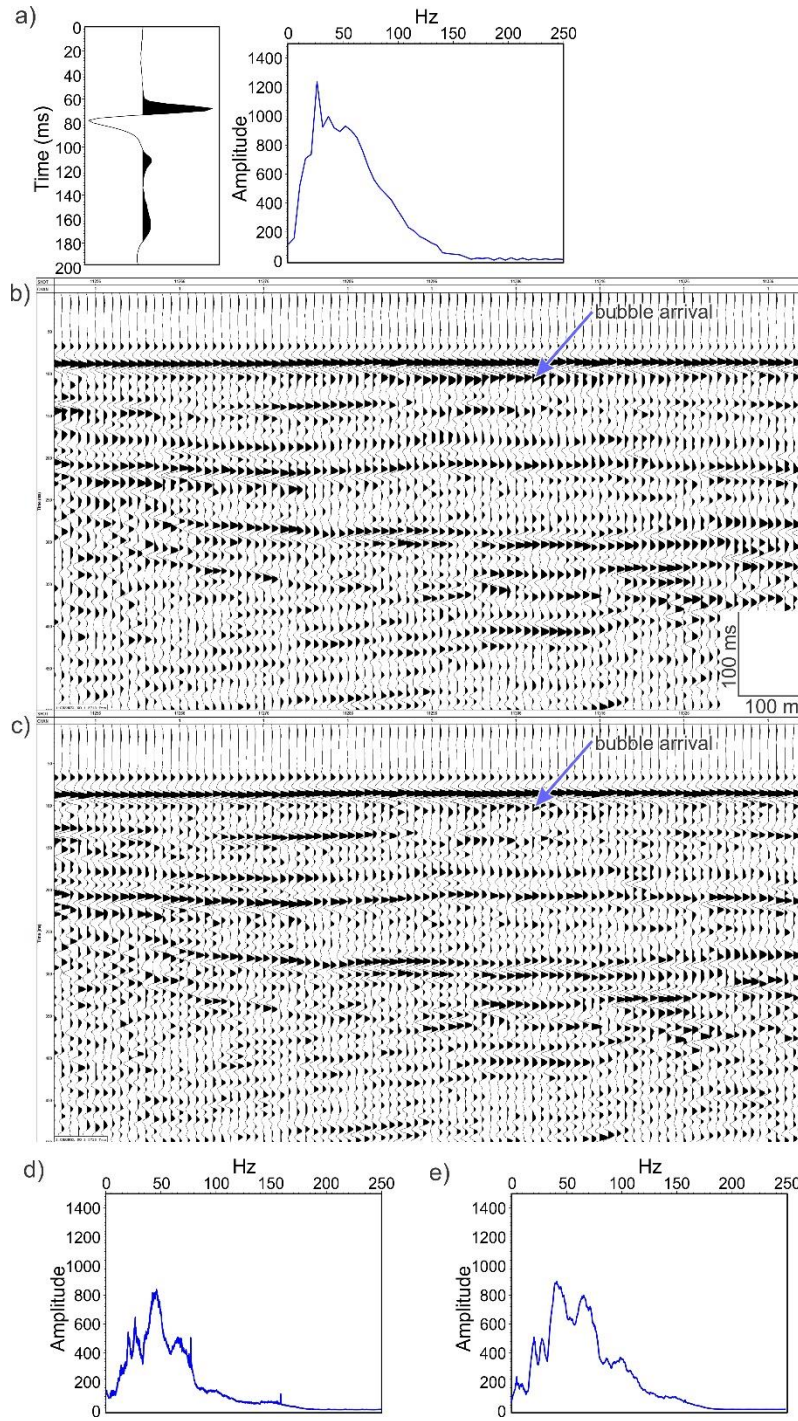
Figure 8. a) Direct arrival extracted at the nearest offset position used to construct the deconvolution operator and its amplitude spectrum, b) common-receiver gather of channel #1 before and c) after source signature deconvolution, d) and e) amplitude spectra before and after source signature deconvolution respectively.
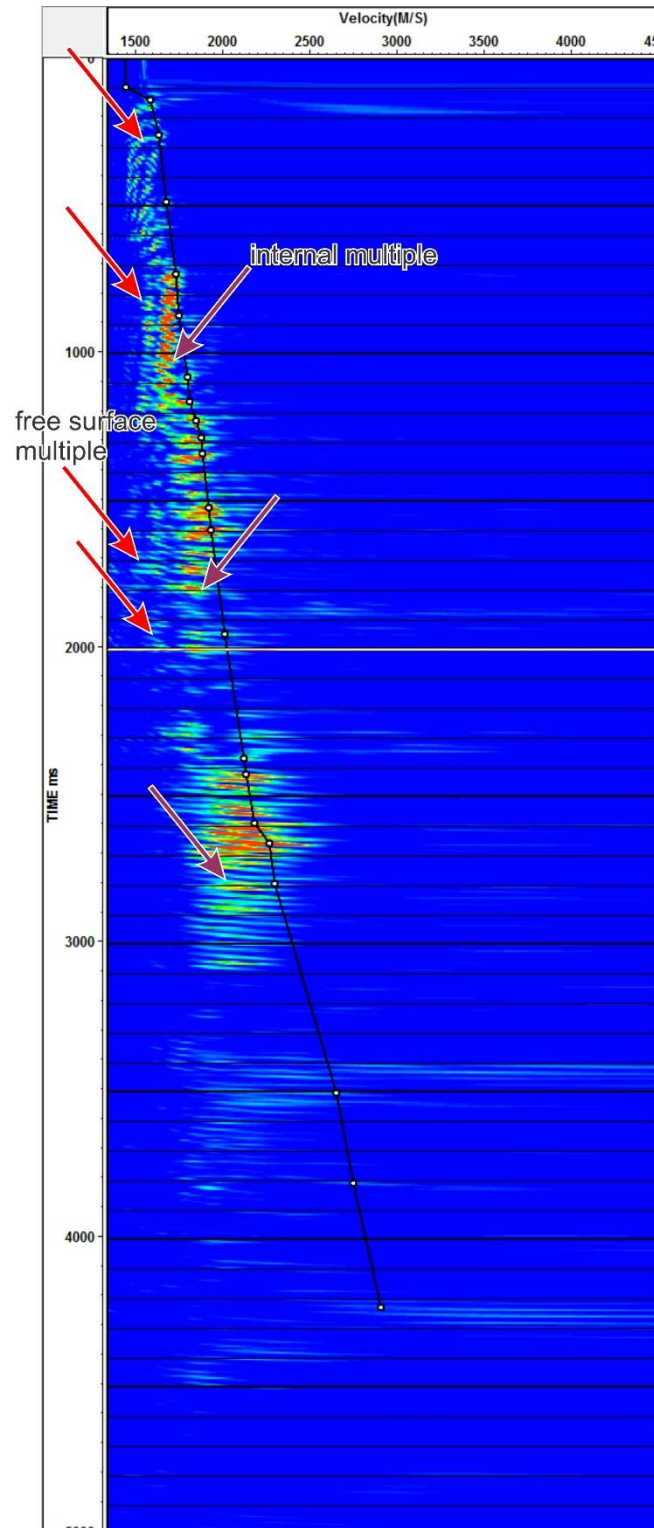
Figure 9. A semblance gather used for the 1st velocity analysis. Dots correspond to velocity picks.

Surface-related multiple attenuation
Surface-related multiple estimation
Two methods were tested to estimate free surface multiples: the method of Verschuur et al. (1992) (i.e. Surface-Related Multiple Elimination) and the method of Foster and Mosher (1992) (i.e. Radon demultiple), both performed in the frequency domain. The first method relies on the autoconvolution of seismic trace from which primary events are transformed into secondary events or multiples. Multiples originating from the source location and recorded at the receiver location are estimated by the autoconvolution of the seismic traces in the common shot gather domain and the common receiver domain. Then, the results of the autoconvolution performed in both domains are summed. The second method exploits the generalized Radon Transform to map seismic events on NMO-corrected CMP gathers in the time of intercept/slope (tau-p) domain from a parabolic integration to isolate surface-related multiple that falls into a different quadrant of the domain compared to the flat events that have been corrected for moveout (for examples see Dunne and Beresford, 1998). After several tests, the method of Foster and Mosher (1992) was selected because of it superior ability to estimate multiples in shallow water depth and hard sea bottom conditions, i.e. in areas of the survey where most high amplitude multiples are generally observed in the data. Figure 10 shows a shot gather recorded in shallow water depth and hard sea bottom condition and predicted multiples for the same shot gather obtained from the parabolic Radon Transform. As expected for this survey, the location of high energy multiples are mostly concentrated between 200 and 600 ms. The yellow arrows on Figure 10a indicate reflected arrivals located between 1000 and 1200 ms having a higher moveout velocity than surface-related multiples, that consequently have not been predicted.

Adaptive subtraction
For directly subtracting the modeled multiples from the data, the traces would require to be 1) perfectly deconvolved for the downgoing wavefield (i.e. the source wavefield) and 2) have the true unit-valued impulse response of the medium (i.e. exact and absolute true amplitude). Obviously, this will never be achieved satisfactorily on real data and justifies the need for adaptive subtraction. Therefore, the estimated multiples are subtracted from the data in an adaptive fashion. Adaptive subtraction involves the computation of an adaptive filter that fits a model trace only including the predicted multiples, to a real trace (Verschuur et al., 1992). The multiple attenuation process is seen as an inversion process where the source and surface reflections are estimated and where the multiple-free data equals the inversion residual. Figure 11 presents the results of multiple attenuation on a common-offset gather (channel #1, 85 m) for data collected in shallow water depth over hard sea bottom. The figure shows that for such difficult acquisition conditions, the method cannot entirely attenuate the multiples but still the results are satisfactory. For easier acquisition conditions, i.e. in greater water depths and over a softer seafloor, the method performs better (Figure 12).
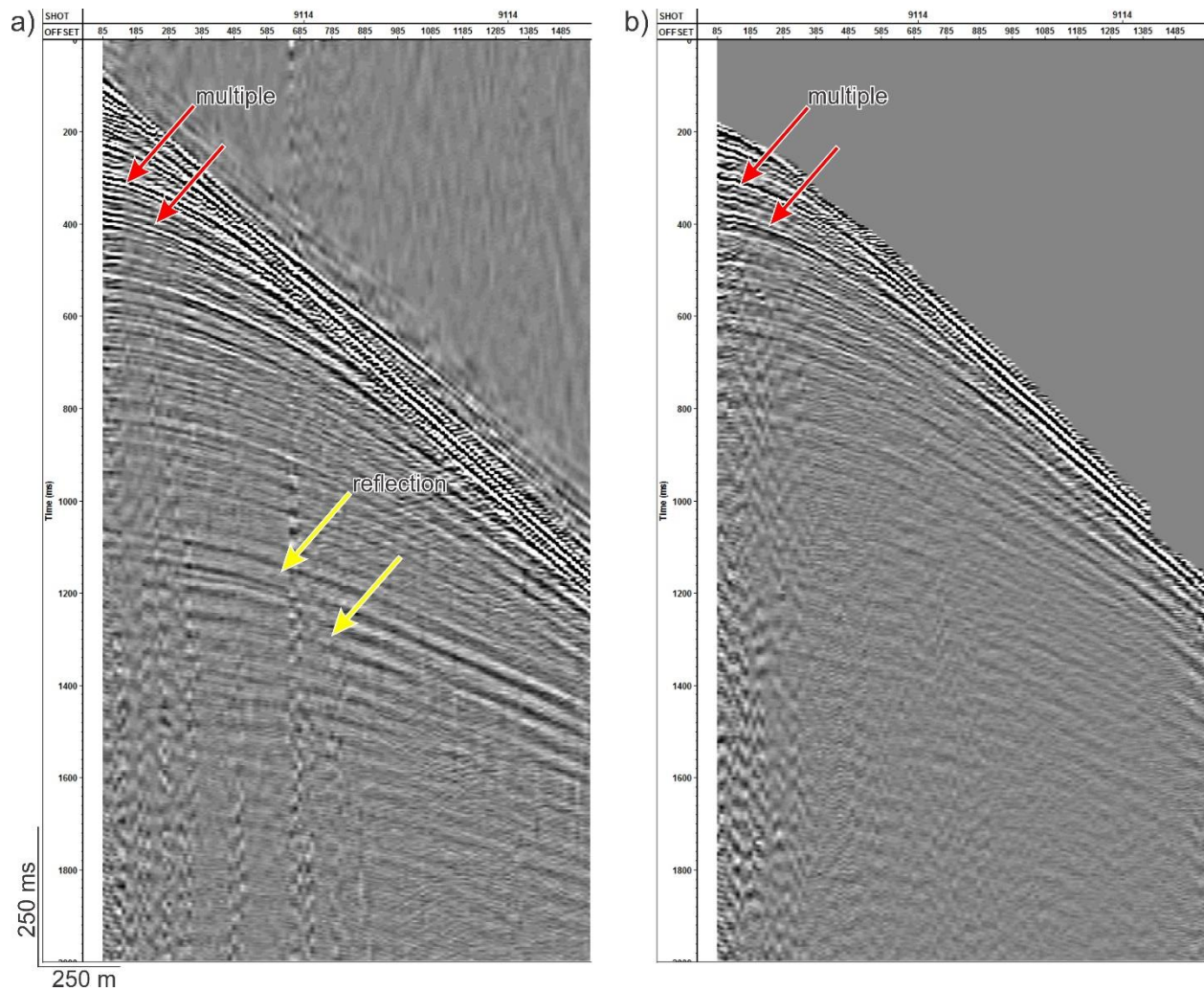
Figure 10. a) Shot gather collected in shallow water and b) corresponding estimated multiples from the parabolic Radon Transform.

2nd velocity analysis

The second velocity analysis is conducted similarly as the first one (see 7.). The purpose of this velocity analysis is to update the initial RMS velocities after multiples are attenuated before velocities are used again for final NMO corrections. Figure 13 compares a semblance gather computed before multiple attenuation (see Figure 9), to a semblance gather computed after multiple attenuation for the same CMP number. Results indicate that semblance markers that are correlative with surface-related multiples now contain less energy, making semblance maxima of the primaries more obvious to pick. Nevertheless, maxima belonging to internal multiples remain.
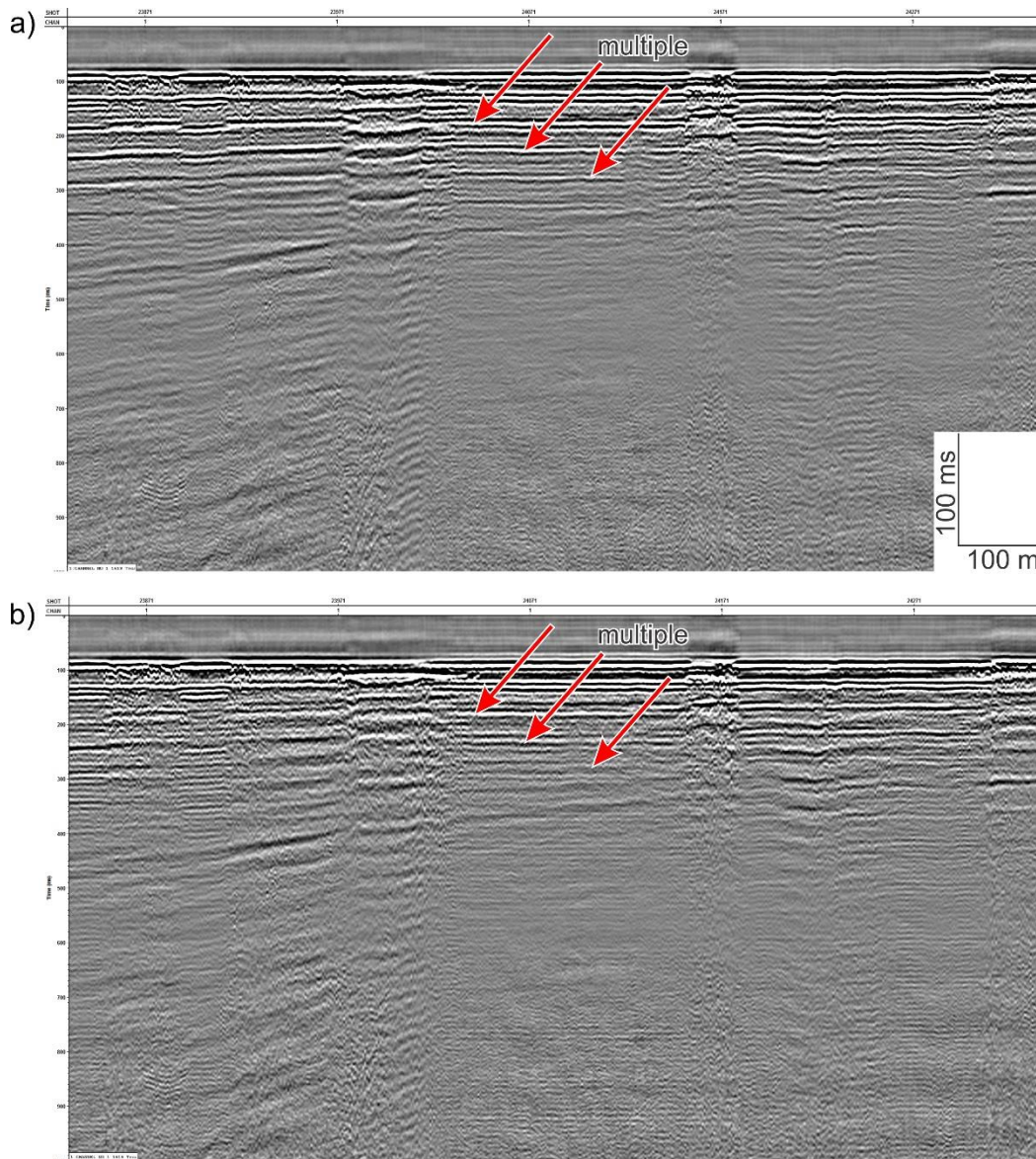
Figure 11. a) Common-receiver gather of channel #1 of data collected in ~60 m of water depth before free surface multiple attenuation and b) after free surface multiple attenuation.

Normal moveout correction

CMP gathers are corrected for normal moveout (i.e. the difference in reflection time because receivers are not located at the source point) using the RMS velocities resulting from the 2nd velocity analysis. This step is done in preparation for time-variant bandpass filtering and random noise attenuation that both perform better on NMO-corrected CMP gathers. Figure 14 presents a 1000 ms time-window of a CMP gather located on line BF10 recorded on the upper continental slope of the Beaufort Sea, the RMS velocity function used to correct the normal moveout and the NMO-corrected CMP gather. The yellow arrow points at a reflection that has been under-corrected. This is most likely because the velocity analysis was conducted every 100 CMPs. Therefore, the velocity function that is applied at this CMP is calculated 221 m away from it. Thus, the velocity field might be slightly different at this CMP location than at the location where the velocity analysis is performed. This will be addressed later by residual moveout corrections.
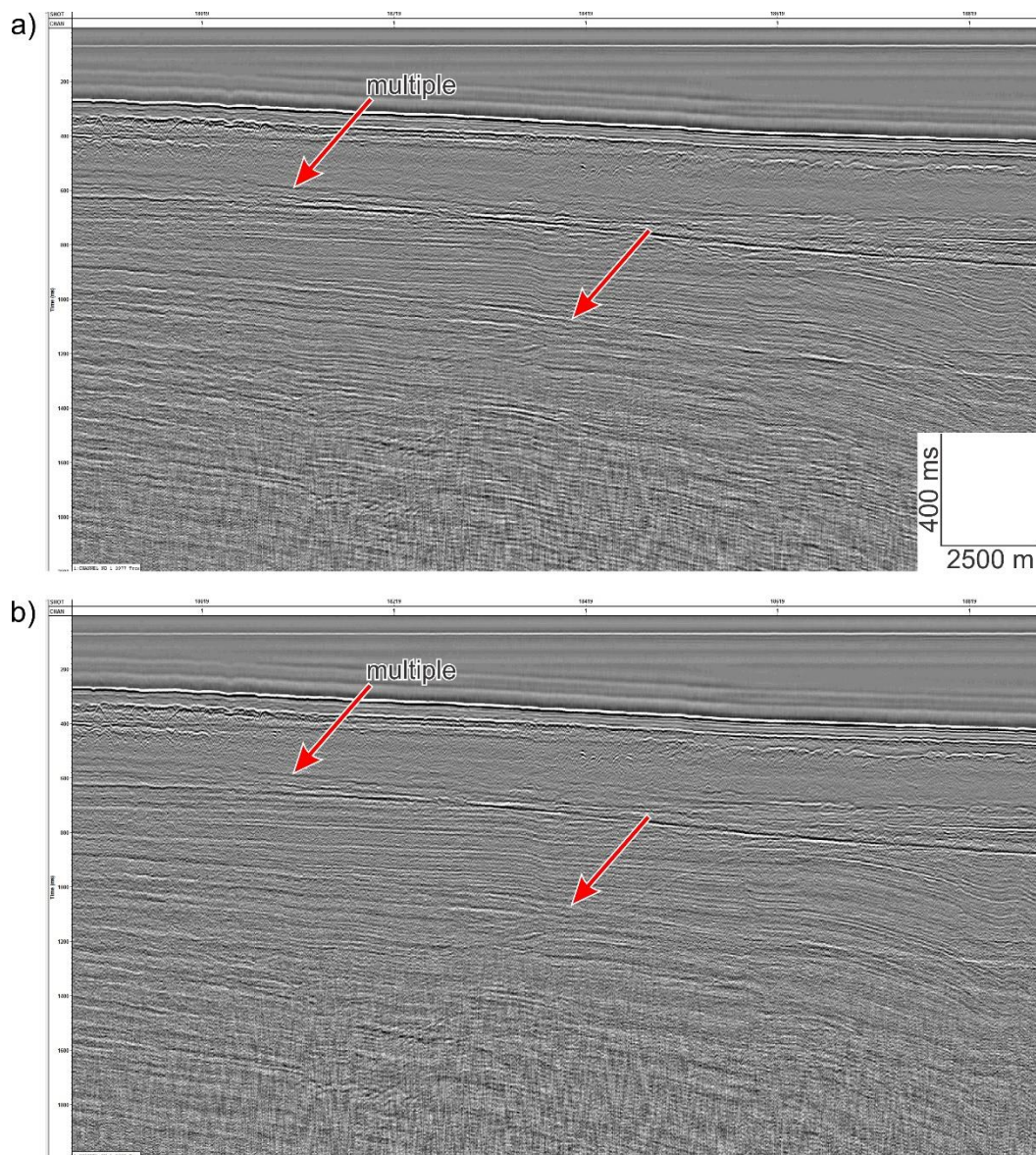
16

Figure 12. a) Common-receiver gather of channel #1 collected in ~180 m of water depth before free surface multiple attenuation and b) after free surface multiple attenuation.

Time-variant filtering
Time-variant filtering (TVF) allowed to change cut-off and corner frequencies of the filters since signal and noise frequency characteristics change as a function of time. Fixed time-windows across lines were mostly used but sometimes time-gates (i.e. time-windows that are not fixed over the entire line) had to be used when large water depth variations occurred along a line. Figure 15
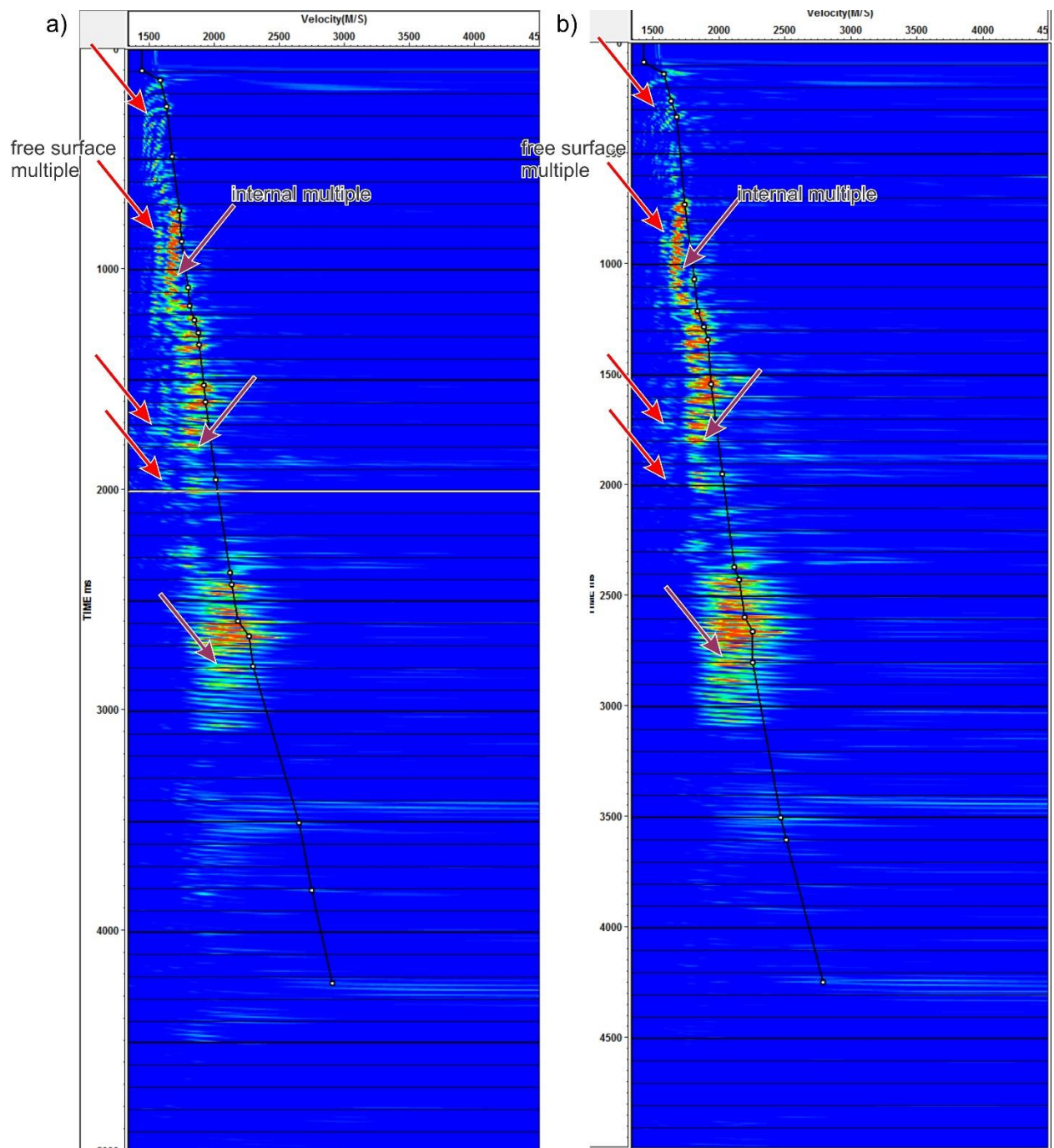
Figure 13. a) A semblance gather before and b) after free surface multiple attenuation. Dots correspond to velocity picks.
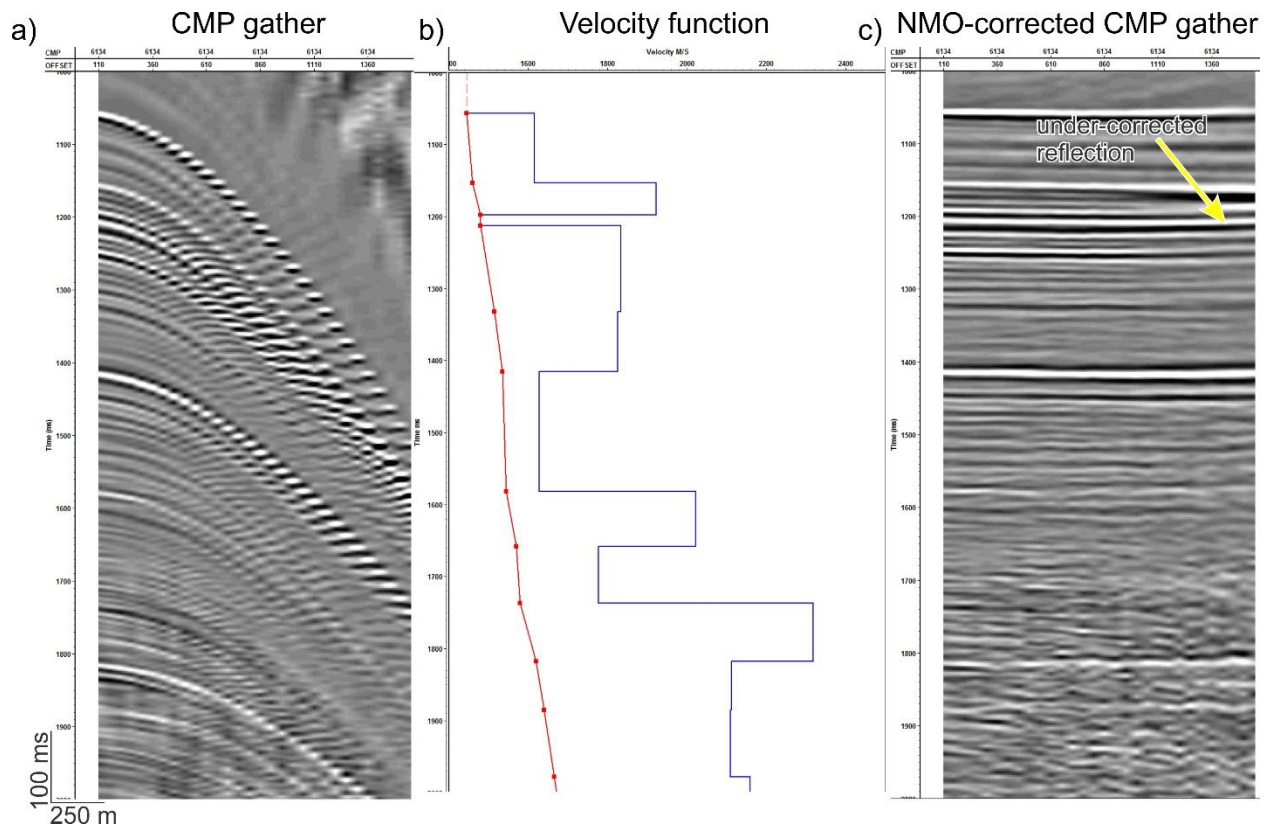
Figure 14. a) A deep-water CMP gather, b) its corresponding velocity function and c) same CMP gather as in a) but after NMO-correction. In b) the red and the blue curves are respectively the RMS velocity and the interval velocity computed from Dix equation (Dix, 1955). The dots on the RMS velocity curve are velocity picks.

illustrates the application of a TVF on a CMP gather located in 65 m of water depth. This example shows the results of a TVF defined as follows: 0-1000ms=5/12/90/120 Hz, 1125-3500ms=5/12/65/90 Hz, 3625-5000ms=5/12/50/60 Hz. Non-overlapping time-windows are used to provide as much as possible a gradual change in the frequency content as a function of time. Figure 15d also presents the amplitude spectrum computed over the 3 different time-windows used to build the TVF showing variations in frequency content and s/n. As expected, after the application of the TVF over each time-window the s/n is increased (Figure 15e).

Random noise attenuation

Here rank reduction is used to attenuate random noise. It is seen as complementary to TVF in order to increase as much as possible the s/n and the coherency of late arrivals before residual moveout correction is applied. Rank reduction is a minimization approach that isolates coherent events having different characteristics. Generally, low-ranks correspond to coherent noise which includes undesired arrivals (e.g. surface waves) and reflections whereas random noise is spread across all
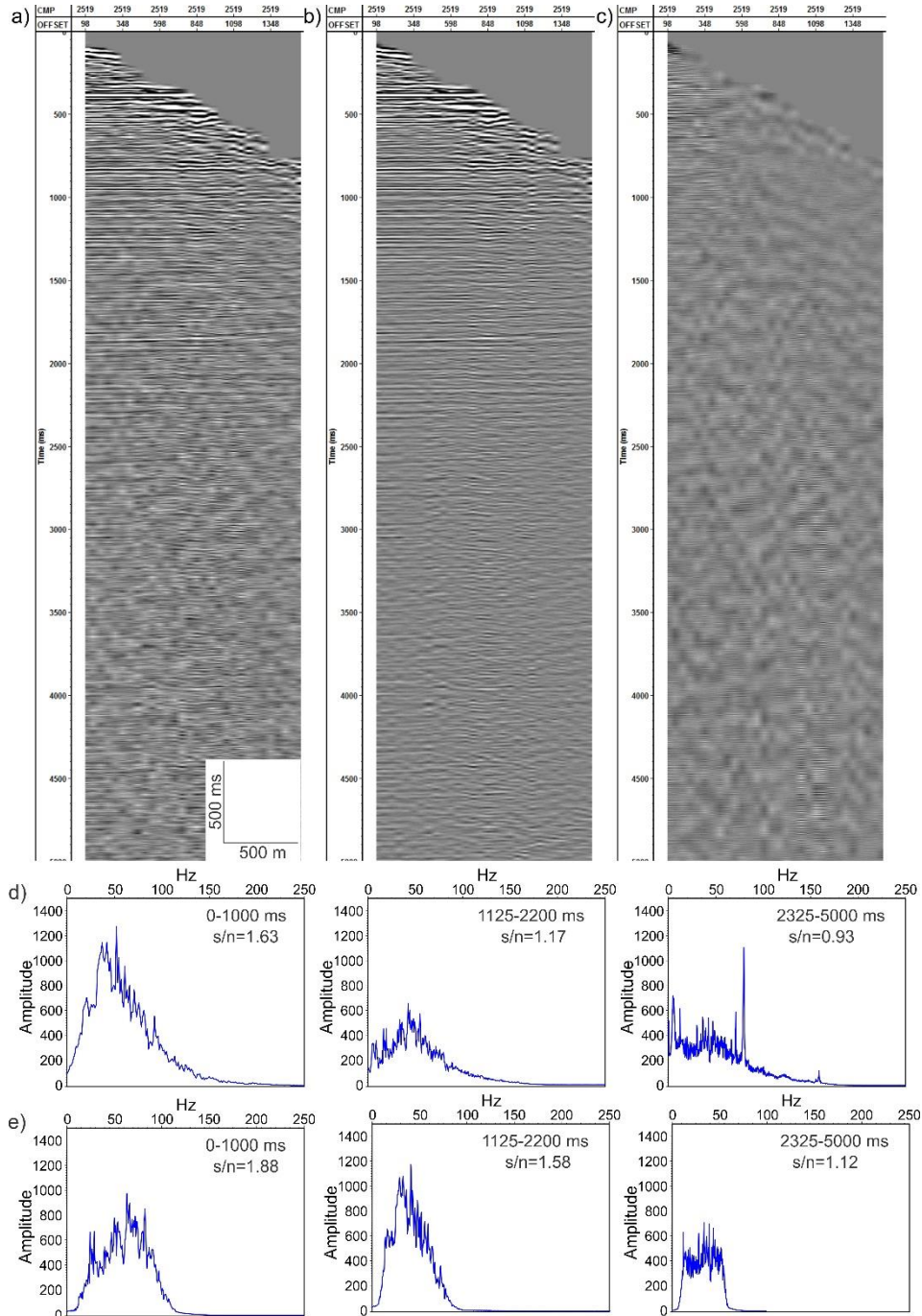
19

Figure 15. a) A NMO-corrected CMP gather before time-variant filtering, b) same as in a) but after TVF, c) difference plot of a)-b), d) amplitude spectra and s/n of the 3 time-windows selected for time-variant filtering and e) same as in d) but after TVF.

ranks. Therefore, the desired signal can be isolated from low-ranks and used to reconstruct data while the undesired random noise is largely attenuated as higher-ranks are eliminated before data reconstruction (Trickett and Burroughs, 2009). The Cadzow (1988) method is applied on the prestack data sorted as shot point gathers. This method is selected because of its proven efficiency

on very noisy datasets and because it preserves AVO effects. Figure 16 illustrates the effect of rank reduction filtering. The reflections within 500 and 2500 ms are more coherent and easier to follow across the offsets after the filtering (see pink box). The amplitude spectra are very similar before and after rank reduction whereas the s/n has significantly increased.
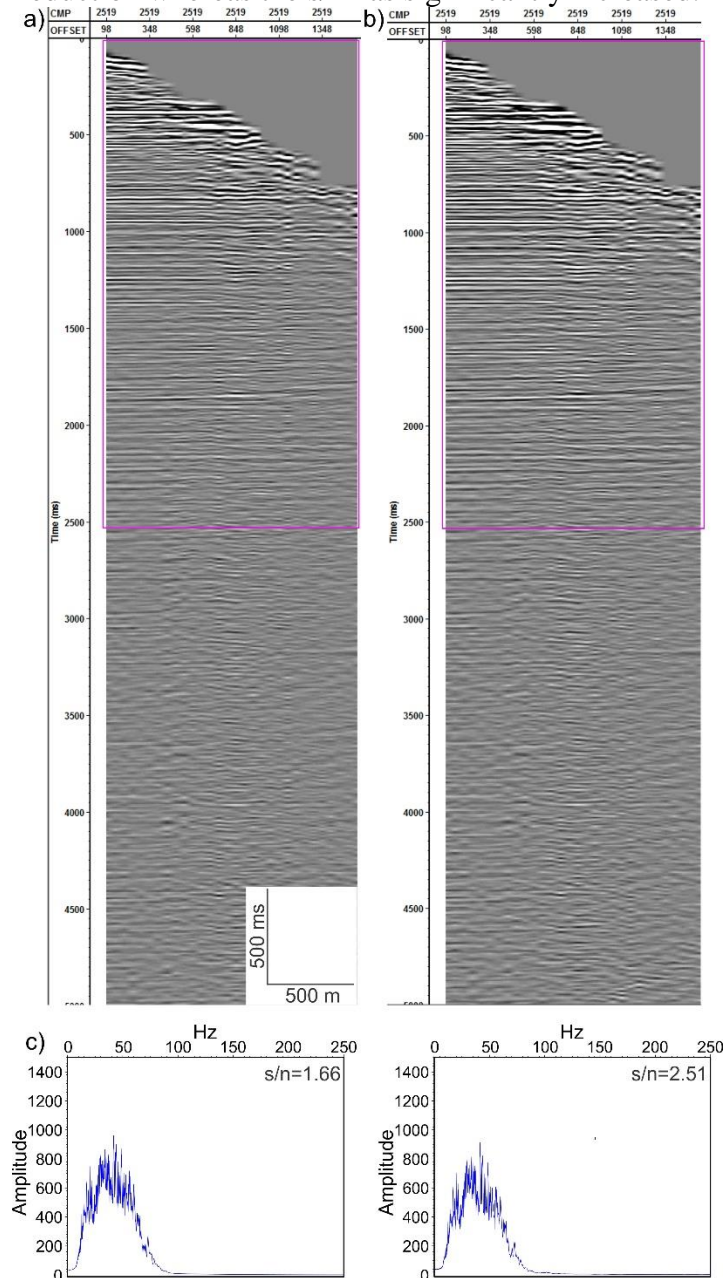

Figure 16. A NMO-corrected CMP gather before (a) and after (b) random noise attenuation. c) From left to right amplitude spectra and s/n of a) and b).

Permafrost breaks attenuation
Additional FK filtering is applied in the shot gather domain to attenuate coherent dipping events known as permafrost breaks, observed in areas of the survey where shallow and fast subsea permafrost exists. These events are attenuated prior to migration to avoid generating artefacts since their velocities are not included in the RMS velocity field initially defined by velocity analysis.

21

Permafrost breaks in prestack seismic data correspond to coherent noise resulting from ice fracturing initiated by the energy released by the seismic source (Merritt, 1974). On Figure 17a, army-green arrows identify some permafrost breaks and the purple arrow indicates residual surface waves also induced by the shallow and fast subsea permafrost. Permafrost breaks have a linear moveout velocity ranging from 2300 to >3000 m s^{-1}. FK filtering adequately attenuated the dipping noise trains of both permafrost breaks and residual surface waves (Figure 17b and c).
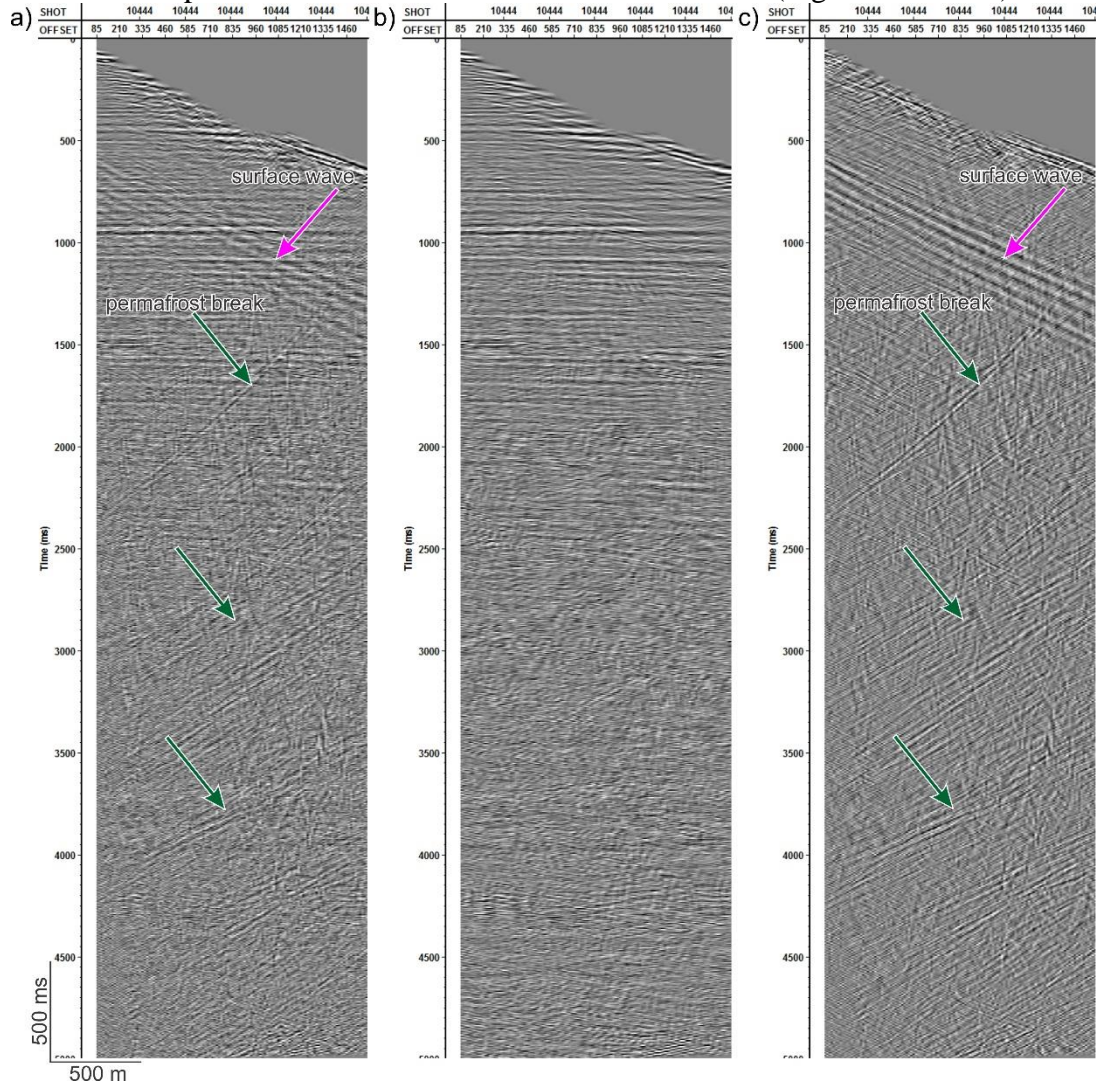

Figure 17. A NMO-corrected shot gather before (a) and after (b) permafrost break attenuation. c) Difference plot of a)-b).

Residual normal moveout correction

This step serves for compensating lateral variations in velocity that cannot be addressed fully since velocity analyses are conducted every 100 CMPs or 625 m. Residual NMO is performed after most of the coherent noise is removed from the data so the efficiency of the process is maximized. This algorithm works by cross-correlating small time-windows of CMP gathers with an optimal stack. Then, the cross-correlation leading to the best stack trace is stored in the data as a time shift. Figure 18 displays results of residual NMO correction on a CMP gather located 237.5 m away from the CMP that is used for velocity analysis. The yellow arrows show two reflections were under-

corrected by the original NMO, which are now flattened by the residual NMO correction. The residual NMO correction used to flatten the reflection at 950 ms and 1181 ms correspond to an increase in velocity of 18 m s^{-1} and 38 m s^{-1} respectively. Some closely-spaced events are also better resolved after residual NMO has been applied (see sand arrows on Figure 18).
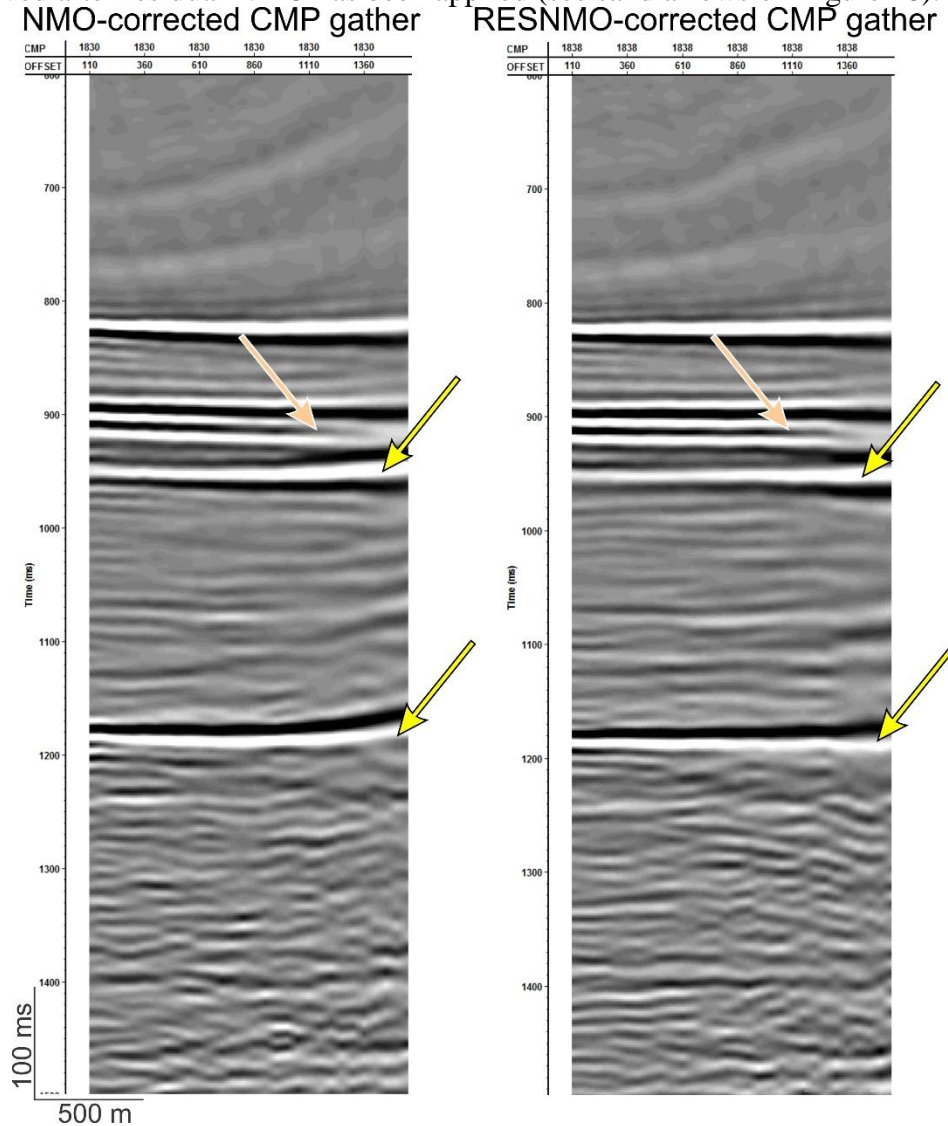

Figure 18. A NMO-corrected CMP gather before (a) and after (b) residual NMO-correction.
CMP stacking

Seismic sections are generated by stacking CMPs. Each seismic trace of the sections results in stacking 30 traces. Some data are stacked later in the processing flow; i.e. when prestack time migration (PSTM) is performed. PSTM is briefly addressed in the discussion and conclusion of this report since it is not systematically conducted on all the lines. Figure 19 compares the brute stack (i.e. a stack section on which a minimum of processing has been done) with a CMP stack after prestack processing on a portion of line BF03 collected in shallow water depths over a hard sea bottom. The section represents 10000 CMPs and 2500 ms. As expected, Figure 19b shows a significant improvement in subsurface imaging in terms of s/n ratio and resolution compared to Figure 19a.
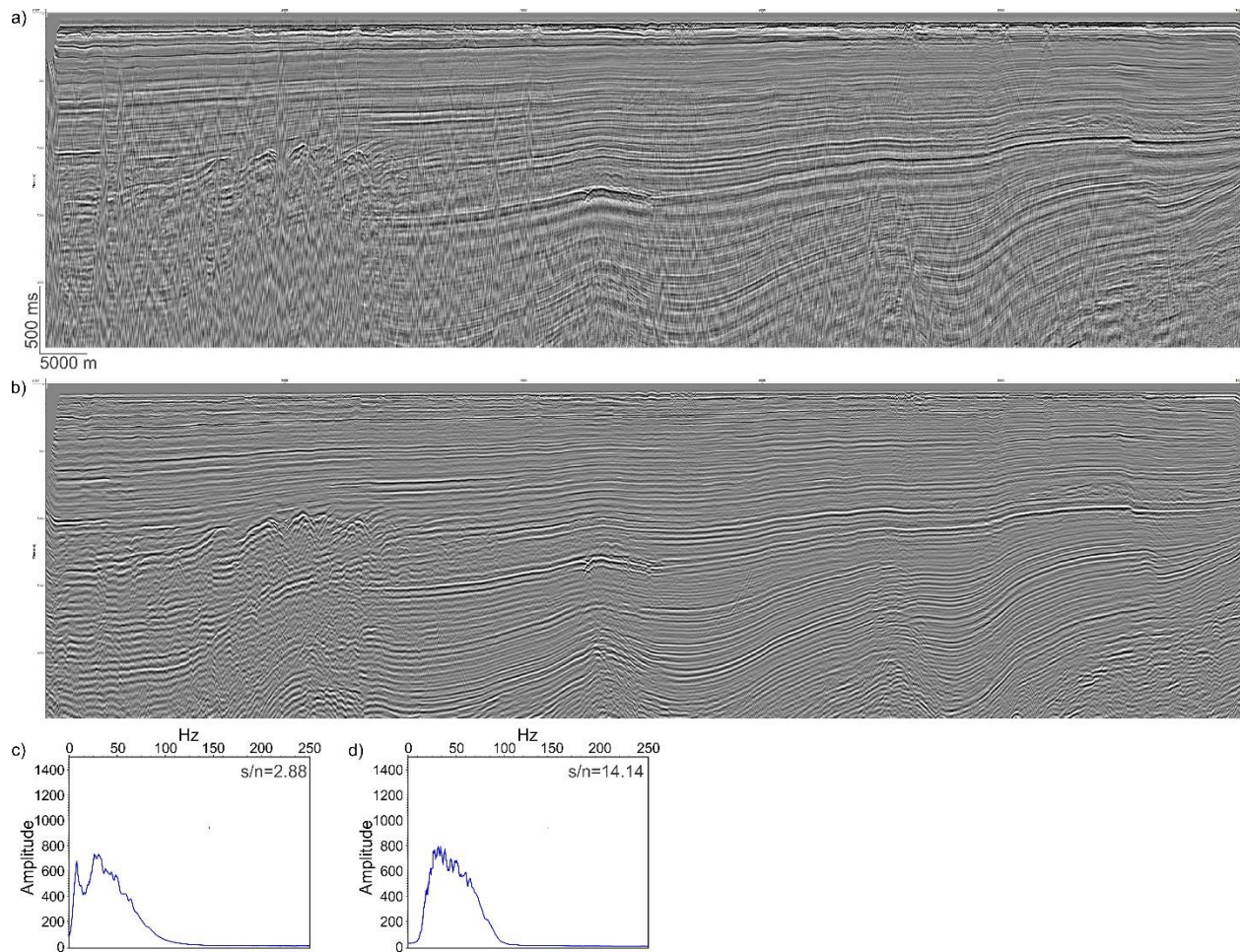
23

Figure 19. A portion of line BF03 collected in ~50 m of water depth. a) Brute stack, b) stack from residual NMO-corrected CMP gathers, c) amplitude spectrum and s/n of a) and d) amplitude spectrum and s/n of b).

Post-stack time migration (PoSTM)

Migration corrects reflected events for dip and variations in velocity causing their recording positions at the surface to be different from their true positions in the subsurface. Stacked sections are migrated using the velocity model updated by residual NMO corrections with the Kirchhoff diffraction sum method (Schneider, 1978). Kirchhoff migration assumes that all raypaths traveling to and from a scatter point go across a time-distance layer with a fixed velocity defined at this scatter point. This approach is selected because it handles complex subsurface geometries, reduces noise by eliminating energy coming from steep dipping reflectors and simply because it is trusted by practitioners. Figure 20 presents migration results over a faulted portion of the subsurface. Migrations successfully collapsed diffracted energy along faults plane allowing a better imaging of these features (see deep-navy blue arrows on Figure 20). Nevertheless, some smiles (i.e. migration artefacts) indicate that the velocity field used for migration is too high over some CMPs (see plum arrows on Figure 20b).

24

Time-variant filtering (TVF)

A second TVF is applied to the data after migration to remove residual high-frequency random noise following an approach similar to the one discussed in 11. Figure 21 shows a portion of line BF01 over a time-distance window of 1200 ms (i.e. 800-2000ms) by 9400 m. On this example, the TVF is set as follows for the entire section: 0-1500ms=5/12/60/90 Hz, 1625-3500ms=5/12/45/65 Hz, 3625-5000ms=5/12/30/45 Hz. The example presents migration noise (plum arrow) that affects the coherency of the reflections (yellow arrow). The TVF considerably attenuated the higher frequency component, increasing the coherency of the reflection pointed by the yellow arrow on Figure 21a and b. The filter is not designed to remove the mid-frequency component of the migration noise since it corresponds to a bandwidth where useful signal is located. The difference plot between a and b indicates that some residual low amplitude and frequency ringing peaking at 9 Hz is removed (army-green arrow) (figure 21c). Figures 21d and e compare the amplitude spectrum before and after TVF. The dashed-line arrow points at the low frequency ringing, the arrow at the 40 Hz-high amplitude component of the migration smile and the double-head arrow at the high frequency noise that is removed.

Time-variant RMS trim-median scaling

A scaling function is applied to balance the amplitudes of the data. Each trace is scaled separately using a time-variant approach. Depending on lines, 3 to 5 time-windows are used over the 5000 ms-long traces. A RMS trim-median function is applied in order to preserve variations on strong amplitude events. This scaling function is computed over a bandwidth that includes the highest s/n, i.e. between 5 and 50 Hz. Figure 22 shows a portion of line BF03 before (a) and after (b) the application of the scaling function. Yellow arrows point at folded structures that are better illuminated after scaling. Figure 23a presents a seismic horizon picked near the top of the section on line BF03. Amplitudes are extracted along the horizon before and after scaling the data. The normalized cross-correlation displayed in b) illustrates that the amplitude of 1 is achieved at sample number 0, meaning that a perfect correlation is obtained between non-scaled and scaled traces. In order words, existing relative amplitude changes time samples are maintained.
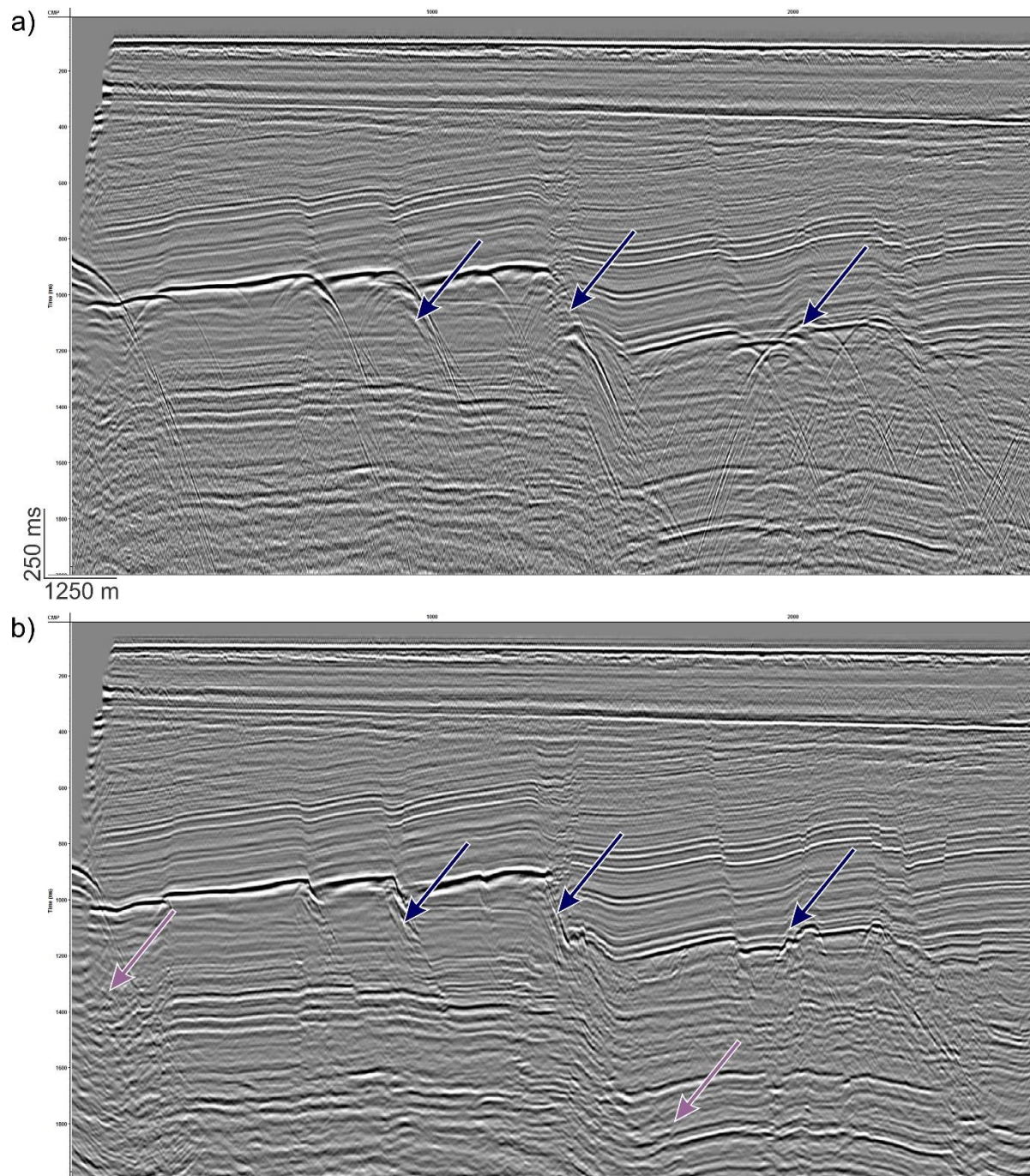
Figure 20. Line BF04 in ~65 m of water depth. a) Stack from residual NMO-corrected CMP gathers and b) PoSTM section.
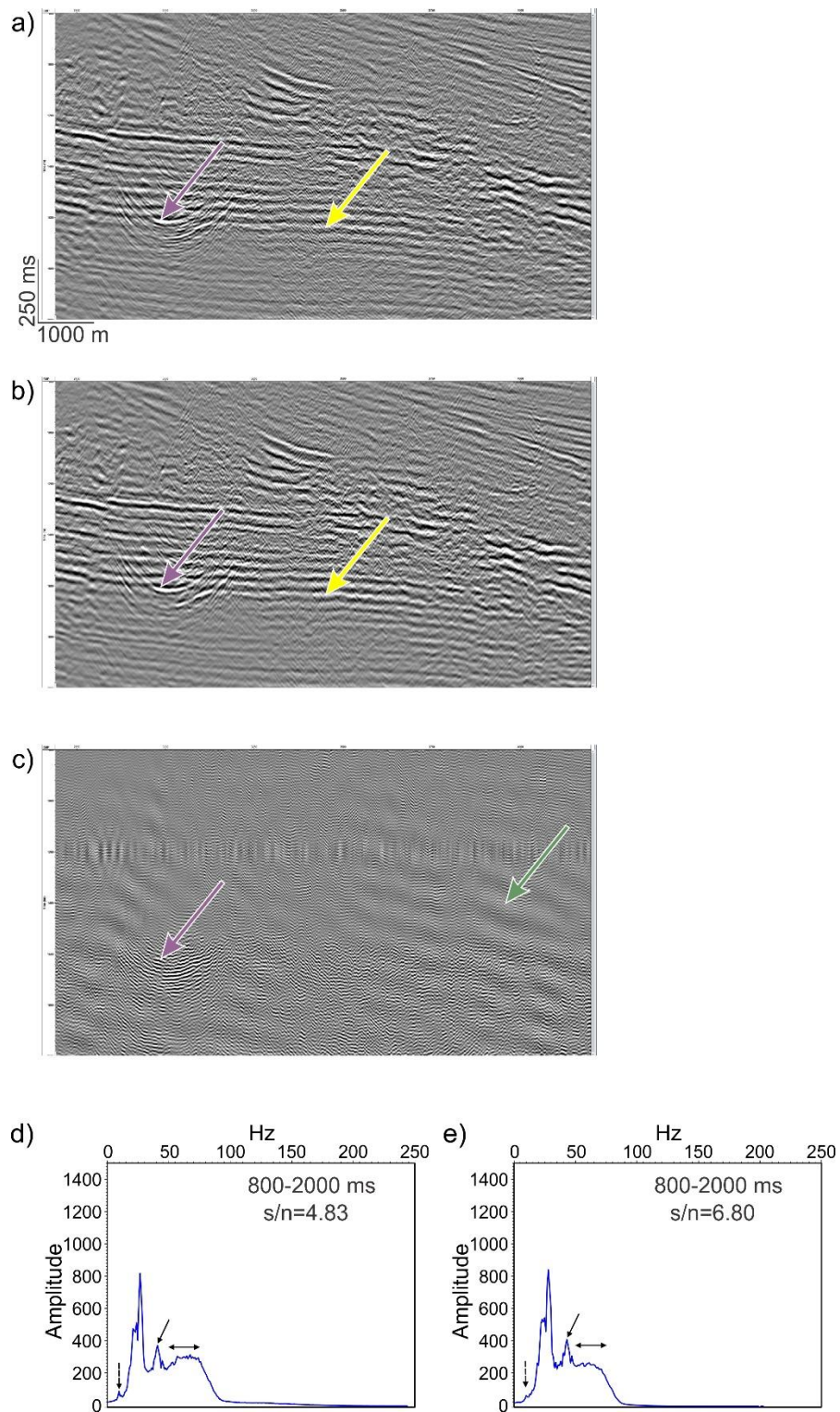
Figure 21. A zoomed-in portion of line BF01. a) Before TVF, b) after TVF, c) difference plot of a)-b), d) amplitude spectrum and s/n before time-variant filtering and e) amplitude spectrum and s/n after time-variant filtering.
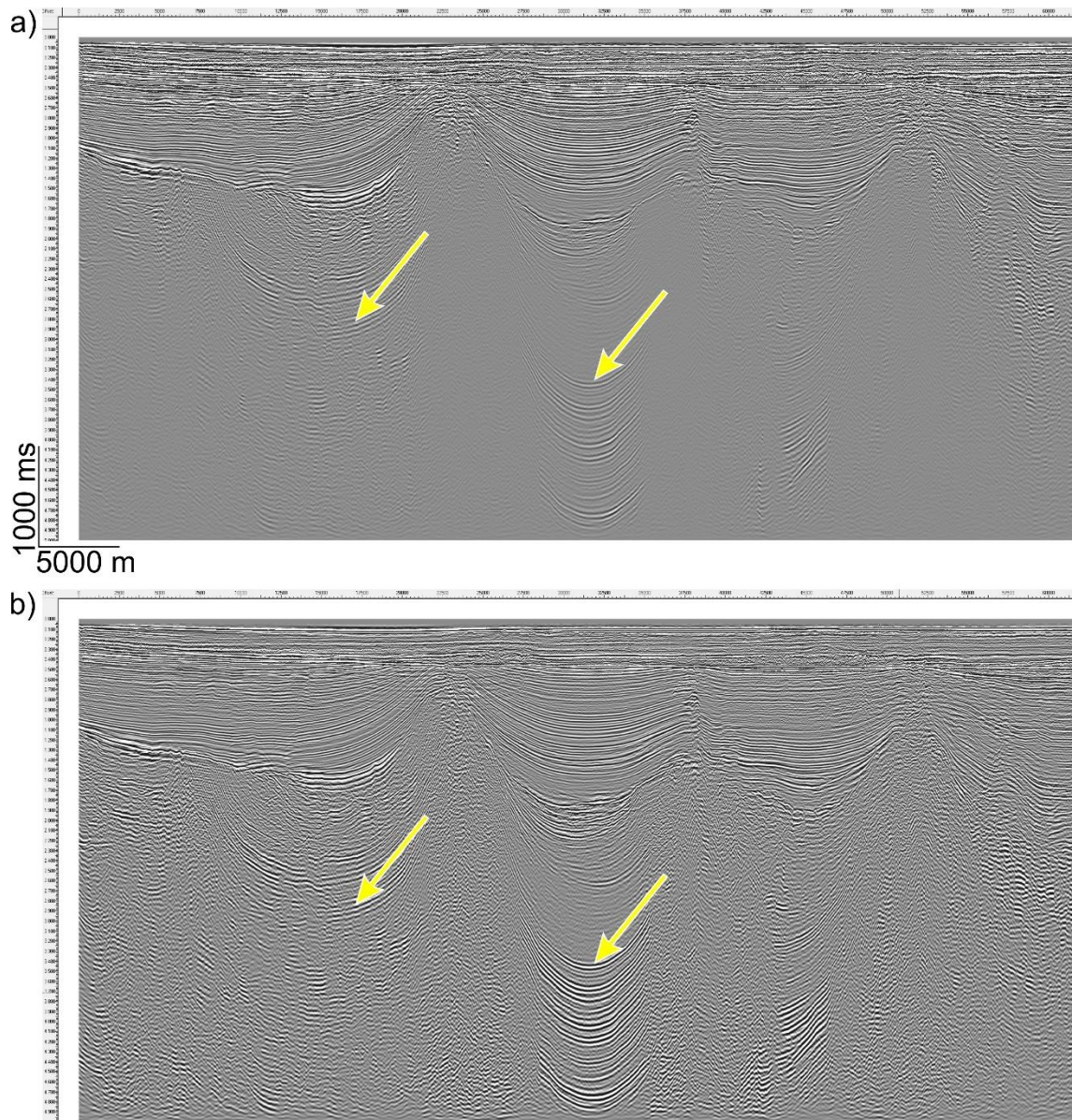
Figure 22. A portion of line BF03. a) Before and b) after time-variant RMS trim-median scaling.

Output data

Data are outputted using the Standard SEG-Y Dictionary in float-32 IBM byte swap format (SEG Technical Committee, 2002). X and Y locations of shot points are written in the 240-byte trace header prior outputting the data. Giving the number of traces per shot gather (i.e. 120) and the CMP fold (i.e. 30) a trace/shot point relationship of 4 is assigned. Additional loading information is listed in Appendix 1.
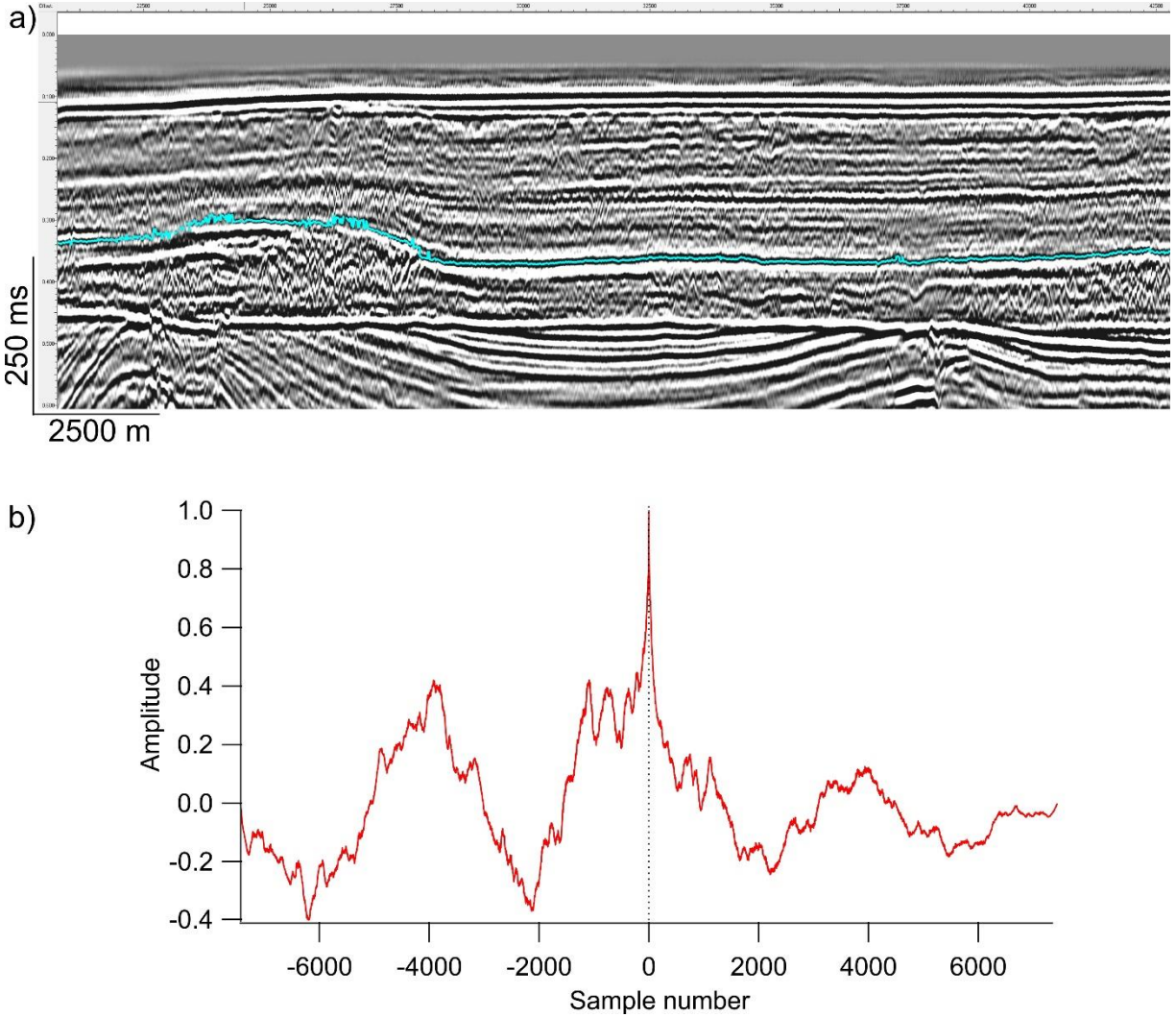
Figure 23. a) Seismic horizon picked near the top of the section on line BF03 and b) normalized cross-correlation between amplitudes extracted along the horizon before and after time-variant RMS trim-median scaling.

DISCUSSION AND CONCLUSION

Figure 24 compares a portion of the brute stack of line BF01 with the fully processed version. The processing flow significantly attenuated random noise leading to a large increase in s/n. Most importantly high energy free surface multiples caused by shallow water depths and hard sea bottom conditions are greatly attenuated (see red arrows). This allows to illuminate geological features that are initially shadowed by the multiples, such as the undulated seismic reflection pointed by the yellow arrows on Figure 24. Nevertheless, some residual multiples exist such as the ones cross-cutting primaries on the processed section. An enhanced multiple attenuation could have probably be achieved by combining the Surface-Related Multiple Elimination method, that proved to be more effective when tested on data collected in deeper water and over softer sea bottom, and the Radon demultiple approach but this would implied a third velocity analysis and therefore significantly lengthen the application of the processing flow.
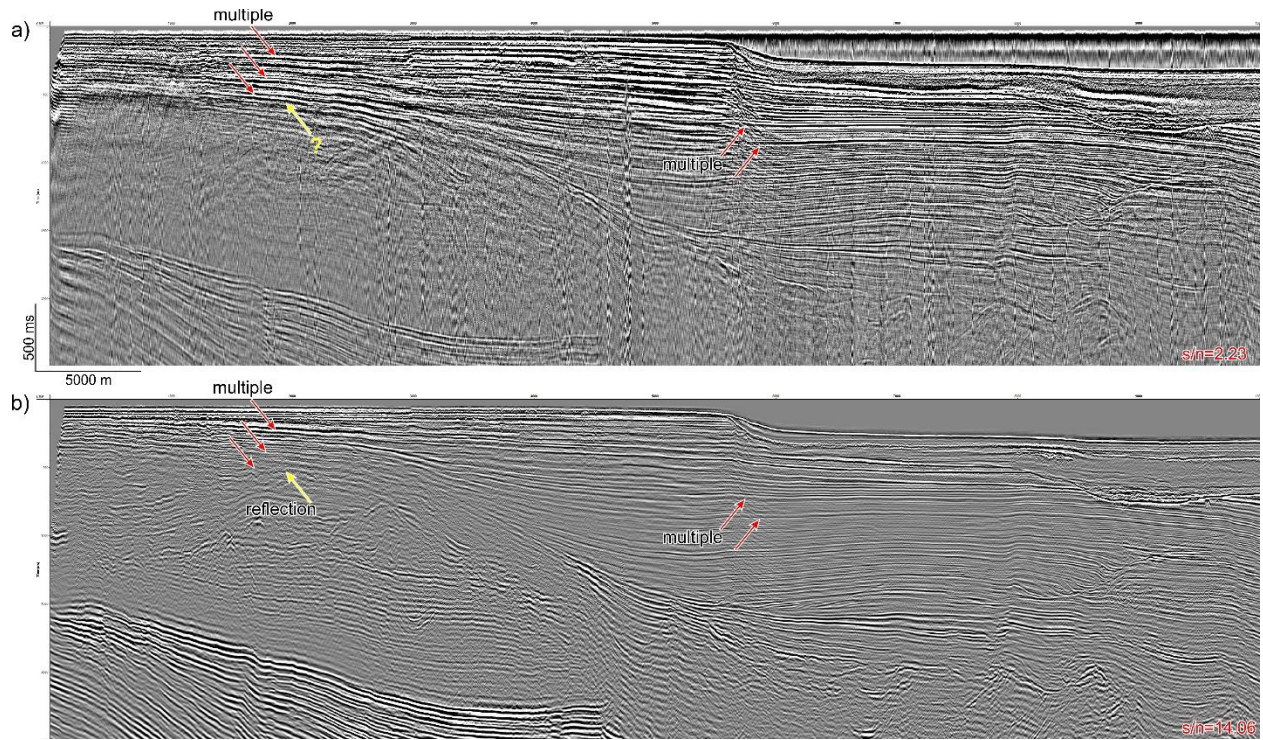
29

Figure 24. A portion of line BF01. a) Brute stack and b) fully processed stack.

PoSTM is performed on the data because it is less time consuming in terms of data preparation than PSTM. However, some PSTM tests conducted on line BF03 proved that, as expected, this method is superior for revealing local or subtle changes embedded within the subsurface. This is because PSTM schemes take into account source and receiver positions of each seismic trace when determining the reflector location as opposed to PoSTM that assumes that source and receiver are both located at the zero-offset position. Figure 25 presents a portion of line BF03 post-stack migrated in a), prestack migrated in b) and the difference between PoSTM and PSTM imaging in c). Even with very modest parametric tests for determining the impulse response of the migrating operator, the PSTM image allows to unveil deeper reflections that are not visible on the PoSTM image (yellow arrows). The fault plane located on the right side of the section also appears sharper as diffractions (deep-navy blue) are more effectively collapsed by the migrating operator. Moreover, more geological details are revealed between 500 ms and the seafloor reflection on the PSTM image. Regardless of the migration scheme, subsurface imaging would benefit from advanced velocity modeling since stacking velocities updated after residual moveout corrections are used to migrate the data.
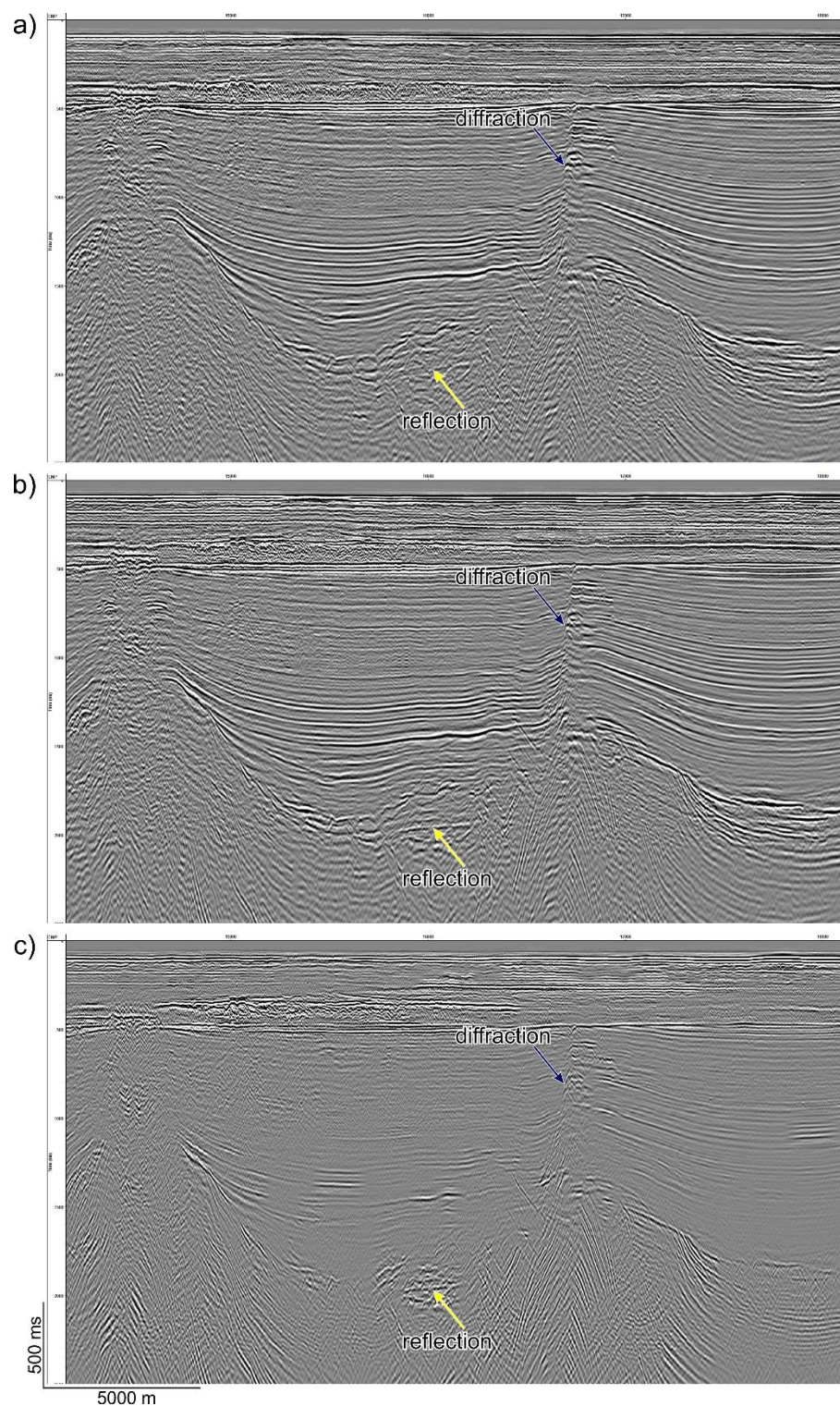
Figure 25. A portion of line BF03. a) PoSTM, b) PSTM and c) difference plot of a)-b).

REFERENCES

Batchelor, C.L., Dowdeswell, J.A., and Pietras, J.T., 2013. Seismic stratigraphy, sedimentary architecture and palaeo-glaciology of the Mackenzie Trough: evidence for two Quaternary ice advances and limited fan development on the western Canadian Beaufort Sea margin. Quaternary Science Reviews, v. 65: p. 73-87.

Blasco, S., Bennett, R., Brent, T., Burton, M., Campbell, P., Carr, E., Covill, R., Dallimore, S., Davies, E., Hughes-Clarke, J., Issler, D., Leonard, L., MacKillop, K., Mazzotti, S., Patton, E., Rogers, G., Shearer, J., and White, M., 2013. 2010 state of knowledge: Beaufort Sea seabed geohazards associated with offshore hydrocarbon development. Geological Survey of Canada, Open File 6989, 340 p.

Butler, P., 2012. Strong noise – removal and replacement on seismic data. CSEG Recorder, v. 37, p. 34-37.

Cadzow, J. A., 1988. Signal enhancement –a composite property mapping algorithm. IEEE Transactions on Acoustics, Speech and Signal Processing, v. 36, p. 49-62.

Dix, C. H., 1955. Seismic velocities from surface measurements. Geophysics, v. 20, p. 68-86.

Dixon, J., Morrell, G.R., Dietrich, J R., Taylor, G.C., Procter, R.M., Conn, R.F., Dallaire, S.M., and Christie, J.A., 1994. Petroleum resources of the Mackenzie Delta and Beaufort Sea. Geological Survey of Canada, Bulletin 474, 126 p.

Dunne, J. and Bresford, G., 1998. Improving seismic data quality in the Gippsland Basin (Australia). Geophysics, v. 63, p. 1496-1506.

Foster, D. J. and Mosher, C. C., 1992. Suppression of multiple reflections using the Radon transform. Geophysics, v. 57, p. 386-395.

Géli, L., Savoye, B., Carton, X. and Stéphan, M., 2005. Seismic imaging of the ocean internal structure: a new tool in physical oceanography? Eos, v. 86, p. 1-10.

Grantz, A., Hart, P.E., and Childers, V.A. 2011. Geology and tectonic development of the Amerasia and Canada Basins, Arctic Ocean. Arctic Petroleum Geology: Geological Society of London Memoirs 35, pp. 771-799.

Graves, J., Chen, Z., Dietrich, J R., and Dixon, J., 2010. Seismic interpretation and structural analysis of the Beaufort - Mackenzie Basin. Geological Survey of Canada, Open File 6217, 22 p.

Helwig, J., Kumar, N., Emmet, P. and Dinkelman, M. G., 2011. Regional seismic interpretation of crustal framework, Canadian Arctic passive margin, Beaufort Sea, with comments on petroleum potential. In Arctic Petroleum Geology, Geological Society Memoirs, volume 35, pp. 527-543.

Jin, Y. K. and Dallimore, S. R., 2016. ARA05C Marine Research Expedition Canada-Korea-USA Beaufort Sea Geoscience Research Program: summary of 2014 activities. Geological Survey of Canada, Open File 7999, 107 p.

Jin, Y. K., Côté, M.M., Paull, C.K. and King, E.L., 2018. 2017 Korea-Canada-U.S.A. Beaufort Sea (offshore Yukon and Northwest Territories) research program: 2017 Araon expedition (ARA08C) cruise report. Geological Survey of Canada, Open File 8406, 206 p.

Jin, Y. K., Riedel, M., Hong, J. K., Nam, S. I., Jung, J. Y., Ha, S. Y., Lee, J. Y., Kim, G. Y., Yoo, J., Kim, H. S., Kim, G., Conway, K., Standen, G., Ulmi, M., and Schreker, M., 2015. Overview of field operations during a 2013 research expedition to the southern Beaufort Sea on the RV Araon. Geological Survey of Canada, Open File 7754, 181 p.

Khatchatrian, V., 2012. Fourier domain regularization 5D and more. CSEG Recorder, v. 37, p. 30-36.

Merritt, R. K., 1974. Seismic reflection measurements in the Canadian Arctic Islands. CSEG: Proceedings of the 1973 National Convention, pp. 89-105.

Newman, P., 1973. Divergence effects in a layered Earth. Geophysics, v. 38, p. 481-488.

Norris, M. W. and Faichney, A. K., 2002. SEG Y rev 1 Data Exchange Format. The Society of Exploration Geophysicists, 45 p.

Pascouet, A., 1991. Something new under the water: the bubbleless air gun. The Leading Edge, v. 10, 79-81.

Paull C.K., Ussler, W. III, Dallimore, S.R., Blasco, S.M. Lorenson, T.D., Melling, H., Medioli, B.E., Nixon, F.M., and McLaughlin, F.A., 2007. Origin of pingo-like features on the Beaufort Sea shelf and their possible relationship to decomposing methane gas hydrates. Geophysical Research Letters, v. 34, L01603. doi.org/10.1029/2006GL027977.

Riedel, M., Brent, T.A., Taylor, G., Taylor, A.E., Hong, J.-K., Jin, Y.-K., and Dallimore, S.R., 2017. Evidence for gas hydrate occurrences in the Canadian Arctic Beaufort Sea within permafrost-associated shelf and deep-water marine environments. Marine and Petroleum Geology, v. 81: p. 66-78.

Schneider, W. A., 1978. Integral formulation for migration in two and three dimensions. Geophysics, v. 43, p. 49-76.

Treitel, S., Shanks, J. L. and Frasier, C. W., 1967. Some aspects of fan filtering. Geophysics, v. 32, p. 789-800.

Trickett, S. and Burroughs, L., 2009. Prestack rank reduction-based noise suppression. CSEG Recorder, v. 34, p. 24-31.

Verschuur, D. J., Berkhout, A. J. and Wapenaar, C. P. A., 1992. Adaptive surface-related multiple elimination. Geophysics, v. 57, p. 1166-1177.

Wood, L. C., Heiser, R. C., Treitel, S. and Riley, P. L., 1978. The debubbling of marine source signatures. Geophysics, v. 43, p. 715-729.

APPENDIX 1: MAIN PROCESSING STEPS

1.INPUT DATA (SHOT GATHERS)
2.GEOMETRY EDITING
3.SPHERICAL DIVERGENCE CORRECTION
4.SWELL NOISE ATTENUATION
5.DIRECT ARRIVAL ATTENUATION
6.SIGNATURE DECONVOLUTION
7.TOP MUTE
8.VELOCITY ANALYSIS PASS 1
9.RADON TRANSFORM MULTIPLE ESTIMATION
10.ADAPTATIVE MULTIPLE ATTENUATION
11.VELOCITY ANALYSIS PASS 2
12.NORMAL MOVEOUT CORRECTION
13.TIME-VARIANT BANDPASS FILTERING
14.RANDOM NOISE ATTENUATION
15.PERMAFROST BREAK ATTENUATION
16.RESIDUAL NMO
17.CMP STACK
18.POST-STACK KIRCHHOFF TIME MIGRATION
19.TIME-VARIANT BANDPASS FILTERING
20.TOP MUTE
21.TIME-VARIANT RMS TRIM-MEDIAN SCALING
22.WRITE XY
23.SEGY OUTPUT
LOADING INFORMATION:
#1: BYTES LOCATION SP=17-20 XY_SCALAR=71-72 X=73-76 Y=77-80
#2: PROJECTED COORDINATE SYSTEM: LAMBERT CONFORMAL CONIC
FALSE_EASTING: 4000000.00000000 METERS
FALSE_NORTHING: 1000000.00000000 METERS
CENTRAL MERIDIAN: -150.50000000 DEGREES
STANDARD PARALLEL 1: 69.16667000 DEGREES
STANDARD PARALLEL 2: 73.83333000 DEGREES
SCALE FACTOR: 1.00000000 DEGREES
LATITUDE OF ORIGIN: 71.50000000 DEGREES
LINEAR UNIT: METERS

APPENDIX 2: ABBREVIATIONS

AGC: Automatic Gain Control
CMP: Common Mid Point
DC: direct current
FFT: Fast Fourier Transform
FK: Frequency-wavenumber
MCS: multichannel seismic
ms: milliseconds
NMO: Normal Moveout
PoSTM: Post-stack time migration
PSTM: Prestack time migration
RMS: Root Mean Square
s/n: signal-to-noise ratio
SEG: Society of Exploration Geophysicists
TVF: Time-variant filtering